PAPER

Check for updates

Glories, hidden rainbows and nearside–farside interference effects in the angular scattering of the state-to-state H + HD → H₂ + D reaction

Chengkui Xiahou [iD] [a] and J. N. L. Connor [iD] ★[b]

Yuan *et al.* [*Nat. Chem.*, 2018, **10**, 653] have reported state-of-the-art measurements of differential cross sections (DCSs) for the H + HD → H₂ + D reaction, measuring for the first time fast oscillations in the small-angle forward region of the DCSs. We theoretically analyse the angular scattering dynamics in order to quantitatively understand the physical content of structure in the DCSs. We study the H + HD($v_i = 0$, $j_i = 0$, $m_i = 0$) → H₂($v_f = 0$, $j_f = 0,1,2,3$, $m_f = 0$) + D reaction for the whole range of scattering angles from $\theta_R = 0°$ to $\theta_R = 180°$, where v, j, m are the vibrational, rotational and helicity quantum numbers respectively for the initial and final states. The restriction to $m_f = 0$ arises because states with $m_f \neq 0$ have DCSs that are identically zero in the forward ($\theta_R = 0°$) and backward ($\theta_R = 180°$) directions. We use accurate quantum scattering matrix elements computed by Yuan *et al.* at a translational energy of 1.35 eV for the BKMP2 potential energy surface. The following theoretical techniques are employed to analyse the DCSs: (a) full and nearside–farside (NF) partial wave series (PWS) and local angular momentum theory, including resummations of the full PWS up to third order. We also use window representations of the scattering matrix, which give rise to truncated PWS, (b) six asymptotic (semiclassical) small-angle glory theories and four N rainbow theories, (c) we introduce "CoroGlo" tests, which let us distinguish between glory and corona scattering at small angles for Legendre PWS, (d) the semiclassical optical model (SOM) of Herschbach is employed to understand structure in the DCSs at intermediate and large angles. Our conclusions are: (a) the small-angle peaks in the DCSs arise mainly from glory scattering. For the 000 → 020 transition, there is also a contribution from a broad, or hidden, N rainbow, (b) at larger angles, the fast oscillations in the DCSs arise from NF interference, (c) the N scattering in the fast oscillation region contains a hidden rainbow for the 000, 020, 030 cases. For the 000 → 020 transition, the rainbow extends up to $\theta_R \approx 60°$; for the 000 and 030 cases, the angular ranges containing a N rainbow are smaller, (d) at intermediate and backward angles, the slowly varying DCSs, which merge into slow oscillations, are explained by the SOM. Physically it shows this structure in a DCS arises from direct scattering and is a distorted mirror image of the corresponding probability *versus* total angular momentum quantum number plot.

1. Introduction

The differential cross section (DCS) for a state-to-state transition in a chemical reaction is a very important observable in a molecular beam experiment, because it contains fundamental information on the dynamics and mechanism of the reaction.[1–4] Recently (in 2018), Yuan *et al.*[5] have reported the first experimental measurements of fast oscillations in the small-angle region for the degeneracy-averaged DCSs of a state-to-state reactive collision. They reported results for the following two transitions in the benchmark reaction (R1)

$$H + HD(v_i = 0, j_i = 0) \rightarrow H_2(v_f = 0, j_f = 1,3) + D \quad (R1)$$

where v_i, j_i and v_f, j_f are the initial and final vibrational and rotational quantum numbers of the diatomic molecules respectively. The experiment used a high-resolution molecular beam apparatus, crossed at 150°, with velocity map imaging product detection for a translational energy of 1.35 eV. These DCS measurements are the current state-of-the-art; related experimental results can be found in ref. 6–9.

In addition, Yuan *et al.*[5] reported an accurate quantum simulation of the experimental degeneracy-averaged DCSs. They observed very good agreement between the theoretical and measured results. The scattering computations of Yuan *et al.*[5] were performed for the helicity-resolved state-to-state reaction

$$H + HD(v_i = 0, j_i = 0, m_i = 0) \rightarrow H_2(v_f = 0, j_f = 0,1,2,3, m_f = 0,1,2,3) + D \quad (R2)$$

[a] *School of Pharmacy, Qilu Medical University, Zibo Economic Zone, Zibo City 255300, Shandong, People's Republic of China*

[b] *Department of Chemistry, The University of Manchester, Manchester M13 9PL, UK. E-mail: j.n.l.connor@manchester.ac.uk; Tel: +44-161-275-4693*

This journal is © the Owner Societies 2021

Phys. Chem. Chem. Phys., 2021, **23**, 13349–13369 | **13349**

where m_i and m_f are the helicity quantum numbers for the initial and final states respectively. Note: it is only necessary to consider non-negative values of m_f in reaction (R2), because the DCSs for $m_f = -1, -2, -3$ are equal to those for $m_f = +1, +2, +3$ respectively. We also note that the scattering amplitude for reaction (R2) can be expanded in a basis set of reduced rotation matrix elements,[5] or equivalently, since $m_i = 0$, in a basis set of associated Legendre functions, $\{P_J^{m_f}(\cos\theta_R)\}$. Here J is the total angular momentum quantum number and θ_R is the reactive scattering angle, *i.e.*, the angle between the incoming H atom and the outgoing H$_2$ molecule in the centre-of-mass reference frame. Thus, $\theta_R = 0°$ and $\theta_R = 180°$ define the forward and backward directions respectively.

The purpose of this paper is to theoretically analyse the dynamics of the angular scattering for the H + HD reaction and to understand the physical content of structure in the DCSs. We consider the whole angular range, $\theta_R = 0°–180°$, not just the small-angle region. Our analyses complement the computer simulation and results in ref. 5.

Before proceeding, we note there is a fundamental difference between the cases $m_f = 0$ and $m_f \neq 0$ for reaction (R2). For $m_f \neq 0$, the scattering amplitudes, and hence the corresponding DCSs, are identically equal to zero at $\theta_R = 0°$ and $\theta_R = 180°$. Only for $m_f = 0$ are the DCSs non-zero in the forward and backward directions; this fact plays a key rôle in our analysis. This result is the consequence of conservation of angular momentum as embodied in the values of reduced rotation matrix elements at $\theta_R = 0°$ and $\theta_R = 180°$. In this paper, we only consider the case $m_f = 0$, with $m_f \neq 0$ analysed in a forthcoming paper. Thus the state-to-state reaction we consider is

$$H + HD(v_i = 0, j_i = 0, m_i = 0) \rightarrow H_2(v_f = 0, j_f = 0,1,2,3, m_f = 0) + D \quad \text{(R3)}$$

There are evidently four state-to-state transitions to be considered for reaction (R3). We will often employ the abbreviations, 000 → 000, 000 → 010, 000 → 020, 000 → 030, or more simply, 000, 010, 020, 030 for these four transitions.

Our analysis will reveal the presence of the following physical phenomena in the DCSs as θ_R increases from 0°: *forward glory* scattering, which can merge into *nearside–farside* fast frequency oscillations, which can include a nearside *broad* or "*hidden*" *rainbow*, which can merge into *direct scattering* exhibiting slow frequency oscillations.

We employ the following theoretical tools in our analysis of structure in the DCSs:

• Partial wave theory

This includes the usual Legendre *partial wave series* for the scattering amplitude, together with a *nearside–farside decomposition*[10–12] and *local angular momentum theory*,[13–16] including *resummations*[13–19] of the partial wave series up to third order. We also make use of *truncated* partial wave series arising from *window representations*[20–22] of the scattering matrix.

• Forward glory scattering theory

To investigate the forward glory, we use the following asymptotic approximations from ref. 23–26: the *integral transitional* approximation, the *semiclassical transitional* approximation, the *primitive* and *classical semiclassical* approximations, and the *uBessel* approximation. We also use the *4Hankel* approximation.[27,28]

Note that we use the words "asymptotic" and "semiclassical" interchangeably, with SC an abbreviation for semiclassical.

• Forward corona scattering theory

Yuan *et al.*[5] drew attention to a qualitative analogy between the fast oscillations in the forward-angle region and the atmospheric corona phenomenon.[29–33] We describe *two tests*, called "CoroGlo", which let us distinguish, for a Legendre partial wave DCS, forward glory scattering from forward corona scattering.

• Nearside rainbow theory

We use the *uniform* and *transitional Airy* approximations;[34] also the *primitive* and *classical semiclassical* approximations (which are different from the ones used for glory scattering).[34]

• Semiclassical optical model

This is a simple approximation for nearside direct scattering introduced by Herschbach.[35,36] It is particularly useful for understanding structure at sideward and backward angles in the DCSs of direct reactions.

This paper is organised as follows. Section 2 outlines the partial wave theory that we use, and explains our conventions and definitions. The properties of the input *scattering matrix elements* are presented in Section 3. The results for the full, nearside and farside DCSs, including resummations, are described in Section 4. Next, in Section 5 we examine the properties of the *quantum deflection function* for the four transitions, as it is fundamental for the asymptotic (semiclassical) theories when they are applied to the scattering amplitudes. The six forward glory theories and their DCSs are described in Sections 6 and 7 respectively. In Section 8, we present the theory of corona scattering, together with the CoroGlo tests, which let us distinguish between glory and corona forward-angle scattering. The extraction of dynamical information from the fast oscillations at small angles in the DCSs is considered in Section 9. Our theories for a nearside rainbow and results are given in Sections 10 and 11 respectively. The theory of the semiclassical optical model is presented in Section 12, with the results for the angular scattering in Section 13. Our conclusions are in Section 14. The effect of resummation on a truncated partial wave series is discussed in the Appendix.

We do not report the results of every theoretical technique mentioned above, as applied to all four state-to-state transitions. Rather we often restrict our detailed discussion to just one transition, if a similar discussion also applies to the other transitions. Most of our results are presented graphically.

2. Partial wave representation

2.1 Partial wave series

Since $m_i = m_f = 0$, the partial wave series (PWS) for the scattering amplitude can be expanded in a basis set of Legendre polynomials

$$f_{000 \to 0j_f 0}(\theta_R)$$

$$= \frac{1}{2ik} \sum_{J=0}^{\infty} (2J+1) S_{000 \to 0j_f 0}^J P_J(\cos(\pi - \theta_R)) \quad j_f = 0,1,2,3$$

$$= \frac{1}{2ik} \sum_{J=0}^{\infty} (2J+1) \tilde{S}_{000 \to 0j_f 0}^J P_J(\cos\theta_R) \quad j_f = 0,1,2,3 \quad (1)$$

13350 | *Phys. Chem. Chem. Phys.*, 2021, **23**, 13349–13369

This journal is © the Owner Societies 2021

The second representation in eqn (1) follows because

$$P_J(\cos(\pi - \theta_R)) = \exp(i\pi J)P_J(\cos\theta_R) \quad J = 0,1,2\ldots$$

and then we write

$$\tilde{S}^J_{000\to 0j_f0} = \exp(i\pi J)S^J_{000\to 0j_f0} \quad J = 0, 1, 2, \ldots$$

where $\tilde{S}^J_{000\to 0j_f0}$ is the Jth modified scattering matrix element. Also, $k \equiv k_{v_i=0, j_i=0}$ is the initial translational wavenumber, J is the total angular momentum quantum number, $P_J(\bullet)$ is a Legendre polynomial of degree J, and θ_R is the reactive scattering angle. In practice, the upper limit of infinity in the PWS is replaced by a finite value, J_{max}, assuming that all partial waves with $J > J_{max}$ are negligible.

The differential cross section (DCS) is then given by

$$\sigma_{000\to 0j_f0}(\theta_R) = |f_{000\to 0j_f0}(\theta_R)|^2 \quad j_f = 0,1,2,3 \quad (2)$$

In our applications, the PWS of eqn (1) contains about 40 numerically significant terms making its physical interpretation difficult or impossible. We also have the estimate, $J_{max} \approx kR$, where R is the reaction radius.

From now on, we will drop the subscript "$000 \to 0j_f0$" to keep the notation simple, and also write $\tilde{S}_J$ in place of $\tilde{S}^J_{000\to 0j_f0}$. In addition, when we continue the set $\{\tilde{S}_J\}$ to real values of J, we will write, $\tilde{S}(J)$; this is required in the SC analyses. Other calculations on the H + HD reaction can be found in ref. 37–42.

We also report results for *truncated* partial wave series (tPWS), which arise when a *window representation* for the S matrix is input into eqn (1). We use as a window the subset, $\{\tilde{S}_J | J = 0 \leq J_i < J_f \leq J = J_{max}\}$, and exclude the case where both $J_i = 0$ and $J_f = J_{max}$. When using a tPWS it is necessary to interpret the resulting tDCS with caution, since partial waves with $J < J_i$ and $J > J_f$ have been neglected, as well as the interference between the partial waves in the window with the two omitted sets of partial waves.

Our results for the H + HD reaction show that the full DCSs calculated from eqn (1) and (2) often exhibit complicated oscillatory structures. To help understand these oscillations, we make a nearside–farside (NF) decomposition of the scattering amplitude. This is outlined next.

2.2 Nearside–farside decomposition

We *exactly* decompose the full scattering amplitude into the sum of two contributing terms, the N and F subamplitudes.[10–12]

$$f(\theta_R) = f^{(N)}(\theta_R) + f^{(F)}(\theta_R) \quad (3)$$

where

$$f^{(N,F)}(\theta_R) = \frac{1}{2ik}\sum_{J=0}^{\infty}(2J + 1)\tilde{S}_J Q_J^{(N,F)}(\cos\theta_R) \quad (4)$$

with $(\theta_R \neq 0,\pi)$

$$Q_J^{(N,F)}(\cos\theta_R) = \frac{1}{2}\left[P_J(\cos\theta_R) \pm \frac{2i}{\pi}Q_J(\cos\theta_R)\right] \quad (5)$$

and $Q_J(\bullet)$ is a Legendre function of the second kind. Similar to eqn (2), the corresponding N and F DCSs are defined by

$$\sigma^{(N,F)}(\theta_R) = |f^{(N,F)}(\theta_R)|^2 \quad (6)$$

Using the asymptotic properties of the $P_J(\bullet)$ and $Q_J(\bullet)$ in the limit $J\sin\theta_R \gg 1$, we obtain, *e.g.*, ref. 19

$$Q_J^{(N,F)}(\cos\theta_R) \sim \left[\frac{1}{2\pi\left(J+\frac{1}{2}\right)\sin\theta_R}\right]^{1/2}\exp\left\{\mp i\left[\left(J+\frac{1}{2}\right)\theta_R - \frac{1}{4}\pi\right]\right\}$$

which is the standard travelling angular wave interpretation.

A local angular momentum (LAM) analysis can also be used to provide information on the total angular momentum variable that contributes to the scattering at an angle θ_R, under semiclassical conditions.[13–16] It is defined by

$$\text{LAM}(\theta_R) = \frac{d\arg f(\theta_R)}{d\theta_R} \quad (7)$$

The same idea can also be applied to the N and F subamplitudes in eqn (3). The corresponding N, F LAMs are defined by[13–16]

$$\text{LAM}^{(N,F)}(\theta_R) = \frac{d\arg f^{(N,F)}(\theta_R)}{d\theta_R} \quad (8)$$

Note that the args in eqn (7) and (8) are not necessarily principal values in order that the derivatives be well defined.

In eqn (4)–(6) and (8), we have used the Fuller NF decomposition,[43] but there are available other NF decompositions for a Legendre PWS, namely those of Hatchell[11,19,44] and Thylwe-McCabe.[45] Note that NF DCS and NF LAM theories have been reviewed by Child (ref. 4, Section 11.2).

2.3 Resummation of the partial wave series

It is known that a resummation[13–19] of the PWS (1) can significantly improve the physical effectiveness of the NF decomposition, (3)–(6). A detailed account of resummation theory for a Legendre PWS has been presented by Totenhofer *et al.*,[19] so we do not repeat this material here.

We have investigated *resummation orders* of $r = 0$ [no resummation, *i.e.*, eqn (1)] and $r = 1$, 2, and 3. We find the biggest effect for *cleaning* the N,F DCSs and N,F LAMs of unphysical oscillations occurs on going from $r = 0$ to $r = 1$. Further resummations, $r = 1$ to $r = 2$, and, $r = 2$ to $r = 3$, have a smaller cleaning effect. Thus in the following we just summarise the $r = 1$ equations. Notice we sometimes label eqn (1) and related un-resummed equations with a subscript, $r = 0$.

Firstly we define

$$a_J = (2J + 1)\tilde{S}_J \quad J = 0,1,2,\ldots \quad (9)$$

then for $r = 1$, the resummed scattering amplitude has the representation[13–19]

$$f(\theta_R) = \frac{1}{2ik}\frac{1}{(1 + \beta_1\cos\theta_R)}\sum_{J=0}^{\infty}a_J^{(r=1)}(\beta_1)P_J(\cos\theta_R) \quad (10)$$

where

$$a_J^{(r=1)}(\beta_1)$$
$$= \beta_1\frac{J}{2J - 1}a_{J-1} + a_J + \beta_1\frac{J+1}{2J + 3}a_{J+1} \quad J = 0, 1, 2, \ldots \quad (11)$$

with $a_{-1} = 0$ from eqn (9). In addition, eqn (10) assumes that $1 + \beta_1 \cos \theta_R \neq 0$. We determine the real, or complex valued, *resummation parameter*, $\beta_1 \equiv \beta_1^{(r=1)}$, in eqn (10) and (11) by solving $a_{J=0}^{(r=1)}(\beta_1) = 0$, which yields $\beta_1 = -3a_0/a_1$. This choice for β_1 is the suggestion of Anni *et al.*[13] A NF decomposition of eqn (10) can also be made. We write

$$f(\theta_R) = f_{r=1}^{(N)}(\beta_1; \theta_R) + f_{r=1}^{(F)}(\beta_1; \theta_R)$$

where the N,F $r = 1$ resummed subamplitudes are given by ($\theta_R \neq 0, \pi$)

$$f_{r=1}^{(N,F)}(\beta_1; \theta_R) = \frac{1}{2ik} \frac{1}{(1 + \beta_1 \cos \theta_R)} \sum_{J=0}^{\infty} a_J^{(r=1)}(\beta_1) Q_J^{(N,F)}(\cos \theta_R)$$

(12)

An alternative form of eqn (12) is[13,19]

$$f_{r=1}^{(N,F)}(\beta_1; \theta_R) = f_{r=0}^{(N,F)}(\theta_R) \mp \frac{1}{2\pi k} \frac{\beta_1 a_0}{(1 + \beta_1 \cos \theta_R)}$$

with $a_0 = \tilde{S}_{J=0}$.

The corresponding N,F $r = 1$ resummed DCSs are then

$$\sigma_{r=1}^{(N)}(\beta_1; \theta_R) = |f_{r=1}^{(N)}(\beta_1; \theta_R)|^2 \qquad (13)$$

and

$$\sigma_{r=1}^{(F)}(\beta_1; \theta_R) = |f_{r=1}^{(F)}(\beta_1; \theta_R)|^2 \qquad (14)$$

respectively. N, F LAMs for $r = 1$ can also be defined by analogy with eqn (8), namely

$$\mathrm{LAM}_{r=1}^{(N,F)}(\beta_1; \theta_R) = \frac{\mathrm{d} \arg f_{r=1}^{(N,F)}(\beta_1; \theta_R)}{\mathrm{d}\theta_R} \qquad (15)$$

Note that the full DCSs and full LAMs for $r = 0$ and $r = 1, 2, 3, \ldots$ are numerically identical. The effect of resummation on tPWS is discussed in the Appendix.

3. Properties of the input scattering matrix elements

The scattering calculations were performed[5] for the Boothroyd–Keogh–Martin–Peterson potential energy surface number two (BKMP2).[46] The numerical S matrix elements were computed by a time-dependent wave-packet method, which uses reactant Jacobi coordinates throughout the wave-packet propagation; also a second-order split operator procedure was employed to propagate the wave packet.[5,38] Converged S matrix elements and DCSs were obtained for translational energies, E_{trans}, up to 3.5 eV.[5]

In this paper, we consider S matrix elements at $E_{\mathrm{trans}} = 1.35$ eV, for the transitions, $000 \to 000$, $000 \to 010$, $000 \to 020$, $000 \to 030$, which is the same translational energy as that employed in the experiments.[5] We use masses of $m_{\mathrm{H}} = 1.0078$ u and $m_{\mathrm{D}} = 2.0141$ u; these correspond to an initial translational wavenumber of $k = 11.692\ a_0^{-1}$. The values of $J_{\max}$ are approximately 40 for each transition.

Fig. 1 shows graphs of $|\tilde{S}_J|$ versus J for the four transitions, with the corresponding four graphs for $\arg \tilde{S}_J/\mathrm{rad}$ versus J
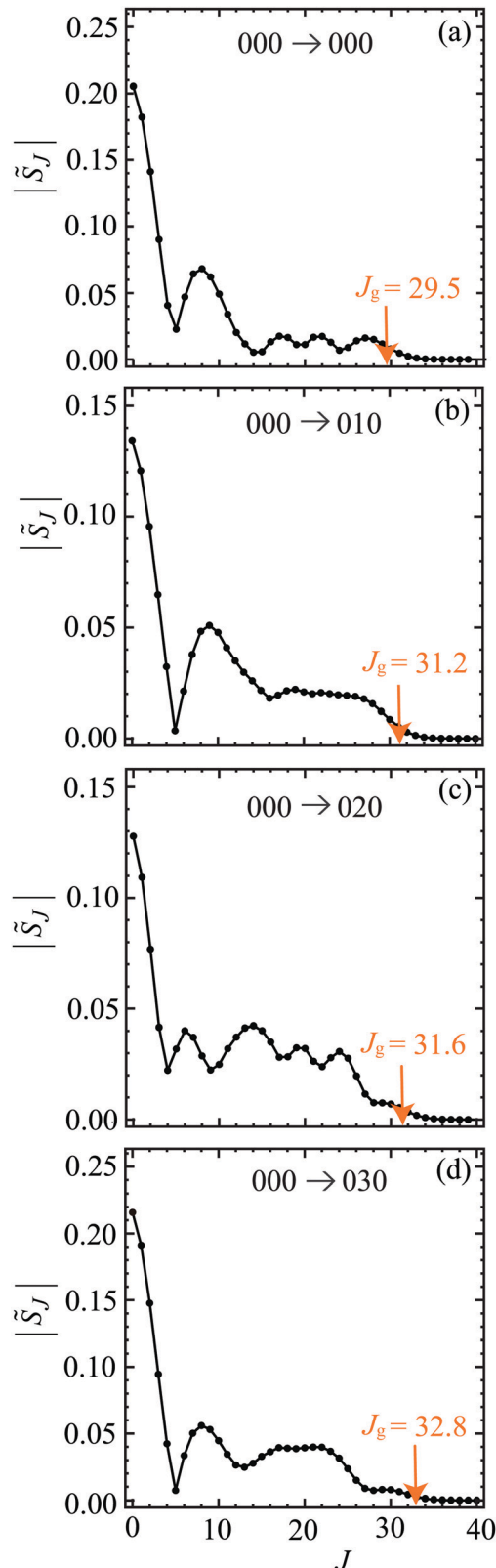

Fig. 1 Plots of $|\tilde{S}_J|$ versus J at $E_{\mathrm{trans}} = 1.35$ eV. The black solid circles are the numerical S matrix data, $\{|\tilde{S}_J|\}$, at integer values of J, which have been joined by straight lines. An orange arrow indicates the value of the glory angular momentum variable, J_{g}. The transitions are: (a) $000 \to 000$, (b) $000 \to 010$, (c) $000 \to 020$, (d) $000 \to 030$.

13352 | *Phys. Chem. Chem. Phys.*, 2021, **23**, 13349–13369

This journal is © the Owner Societies 2021

displayed in Fig. 2. On inspection of Fig. 1 and 2 we note the following:

• The maximum for a $|\tilde{S}_J|$ plot occurs at $J = 0$ for all four transitions. As J increases, there are up to four noticeable subsidiary maxima. It can be seen that the first minimum occurs at $J = 5, 5, 4, 5$ for the 000, 010, 020, 030 cases respectively. The shapes of the $|\tilde{S}_J|$ plots at low J play an important rôle in explaining structure in the DCSs at sideward and backward angles using the SOM theory, as will be demonstrated in Section 13. The relatively complicated shapes of the $|\tilde{S}_J|$ plots are typical of other reactions involving H and D, for example, the $H + D_2 \rightarrow HD + D$ reaction.[23,24]

• The plots of $\arg \tilde{S}_J$/rad *versus* J are seen to be roughly quadratic in shape. The positions of the broad *local maxima* define the glory angular momentum variable, J_g, which has values in the range 29.5 to 32.8 for the four transitions. These values of J_g, are marked on Fig. 1 and 2, where it can be seen that $|\tilde{S}(J_g)|$, and also $(2J_g + 1)|\tilde{S}(J_g)|$, are not negligible. These results imply that J_g will be an important variable in the asymptotic (or SC) analysis of glory scattering in Sections 6 and 7. Also visible in Fig. 2 are *kinks* in the curves for the 000, 010, 030 cases. They occur when the corresponding $|\tilde{S}(J)|$ has a near-zero and the phase of $\tilde{S}(J)$ then varies more rapidly with respect to J.

4. Full and nearside–farside DCSs including resummations

Fig. 3 shows logarithmic plots of the full and N, F $r = 1$ DCSs *versus* θ_R for the four transitions. We use the following colour conventions for the DCSs, and in some other figures:

• Full PWS: black solid, with the label, PWS.
• N $r = 1$ PWS: red solid, with the label, PWS/N/$r = 1$.
• F $r = 1$ PWS: blue solid, with the label, PWS/F/$r = 1$.

The full DCS for the 000 → 000 transition is seen to exhibit the following properties as θ_R increases from 0° to 180°:

• A forward peak at $\theta_R = 0°$, which merges into fast frequency oscillations, which damp out at $\theta_R \approx 50°$.

• An angular region extending from $\theta_R \approx 50°$ to $\theta_R \approx 100°$, where the DCS varies more slowly.

• An angular region from $\theta_R \approx 100°$ to $\theta_R = 180°$, where there are pronounced slow frequency oscillations.

The DCSs for the other three transitions exhibit similar properties to the 000 case.

Next we examine the N, F $r = 1$ DCSs. Using the *fundamental identity for N,F DCSs*, *e.g.* ref. 19, we obtain important insights into structure occurring in the full DCSs. The fast frequency oscillations at forward angles, together with the forward peak are seen to arise from NF interference. Note that the variation of the N and F $r = 1$ DCSs with θ_R is slower than that for the corresponding full DCS. This behaviour is typical of glory scattering.[24–26] It will be proven in Sections 6 and 7 using asymptotic techniques that the forward peak is indeed mainly a glory. The NF oscillations have a physical interpretation similar to the interference pattern from the well-known
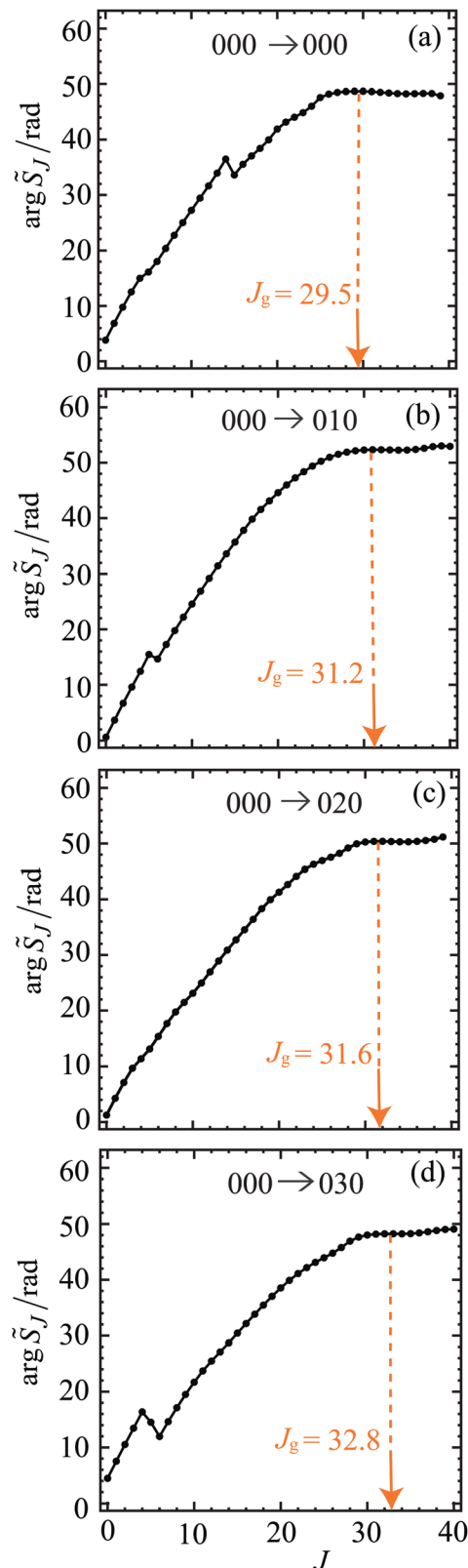

Fig. 2 Plots of $\arg \tilde{S}_J$/rad *versus* J at $E_{trans} = 1.35$ eV. The black solid circles are the numerical S matrix data, {$\arg \tilde{S}_J$/rad}, at integer values of J, which have been joined by straight lines. An orange dashed line and orange arrow indicates the value of the glory angular momentum variable, J_g. The transitions are: (a) 000 → 000, (b) 000 → 010, (c) 000 → 020, (d) 000 → 030.

This journal is © the Owner Societies 2021

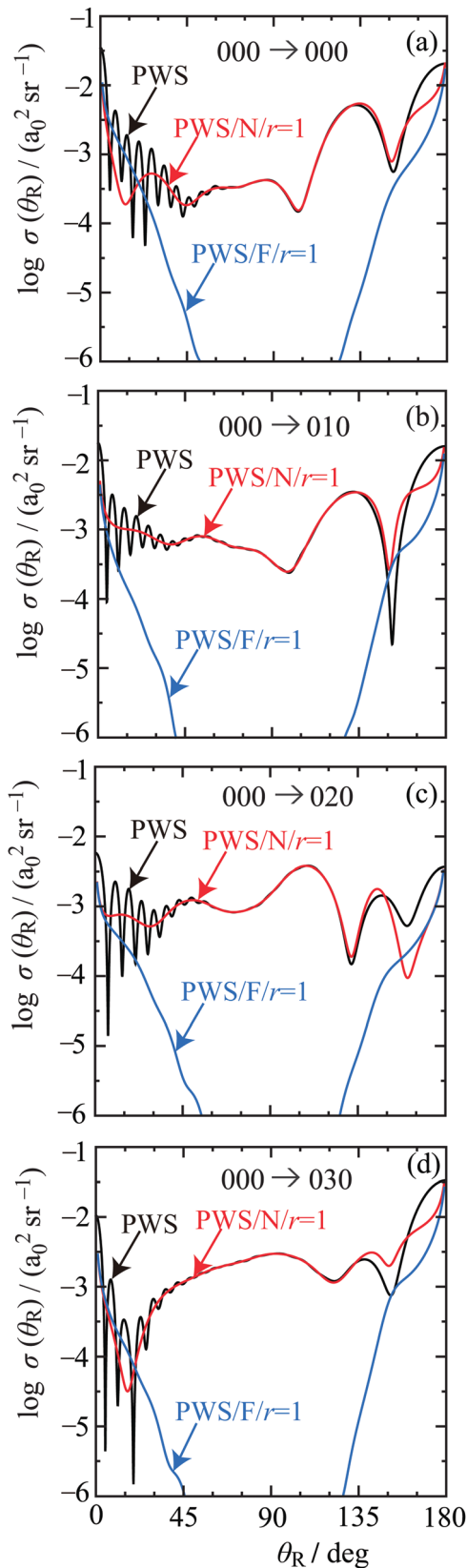*Phys. Chem. Chem. Phys.*, 2021, **23**, 13349–13369 | **13353**

Fig. 3 Plots of $\log \sigma(\theta_R)$ *versus* θ_R at $E_{trans} = 1.35$ eV for: full PWS (black curve), N $r = 1$ PWS (red curve), F $r = 1$ PWS (blue curve). The transitions are: (a) 000 → 000, (b) 000 → 010, (c) 000 → 020, (d) 000 → 030.

"Young's double slit" experiment – see Appendix A of ref. 47 for more details of this analogy in a scattering context. A useful result from this analogy is a simple approximate formula for the period of the oscillations, denoted $\Delta\theta_R$, namely

$$\Delta\theta_R/\text{rad} \approx \pi/J_{eff} \qquad (16)$$

where J_{eff} is an effective total angular momentum variable giving rise to the NF interference oscillations.

In contrast, the scattering at sideward and backward angles is N dominated. Thus the NF analysis tells us the important result that the oscillations at forward and backward angles arise from different physical mechanisms. The results for the full and N, F $r = 1$ LAMs are consistent with those for the DCSs and are not shown.

To proceed further we need to undertake the much more difficult task of constructing the asymptotic (or SC) limit of the full and N, F PWS for each transition. This requires we first examine the properties of the *quantum deflection functions*, which are considered next.

5. Quantum deflection functions and their properties

The PW theory in Sections 2–4 uses the set of S matrix elements, $\{\tilde{S}_J\}$, with $J = 0, 1, 2,\ldots, J_{max}$. The asymptotic theory presented in Sections 6–13 requires the continuation of $\{\tilde{S}_J\}$ to real values of J, which we denote by $\tilde{S}(J)$. That is, the S matrix elements are now considered to be a continuous function of the total angular momentum variable, J.

An important rôle in the SC analysis is played by the *quantum deflection function* (QDF), denoted $\tilde{\Theta}(J)$, and defined by

$$\tilde{\Theta}(J) = \frac{d \arg \tilde{S}(J)}{dJ} \qquad (17)$$

As for eqn (7) and (8), the arg in eqn (17) is not necessarily the principal value in order that the derivative be well defined (ref. 24 explains how to construct numerically the $\tilde{\Theta}(J)$ curves).

Fig. 4 shows graphs of $\tilde{\Theta}(J)/\text{deg}$ *versus* J for the four transitions. Cubic B-spline interpolation was usually used for the continuation of $\{\tilde{S}_J\}$ to $\tilde{S}(J)$. Inspection of Fig. 4 reveals the following:

• The curves for $\tilde{\Theta}(J)/\text{deg}$ *versus* J are rather complicated with many maxima and minima.

• The most striking feature in the QDF plots are the steep *dips*, which occur for the 000, 010, 030 transitions. The minima of these dips occur for $J \approx 14.5, 5.5, 5.1$ respectively and are evidently associated with the kinks in the $\arg\tilde{S}_J/\text{rad}$ plots of Fig. 2. Do we see noticeable structure in the DCSs associated with these dips? Inspection of Fig. 3 shows that the answer is *no*. We can understand this result because the contribution to a SC DCS, *e.g.* using the stationary phase approximation, is typically proportional to $1/|d\tilde{\Theta}(J)/dJ|$. Now the moduli of the slopes are very large for a steep dip (except close to its minimum) and their contribution to the SC DCS will be very small. In addition, the two branches for each dip are separated by only a
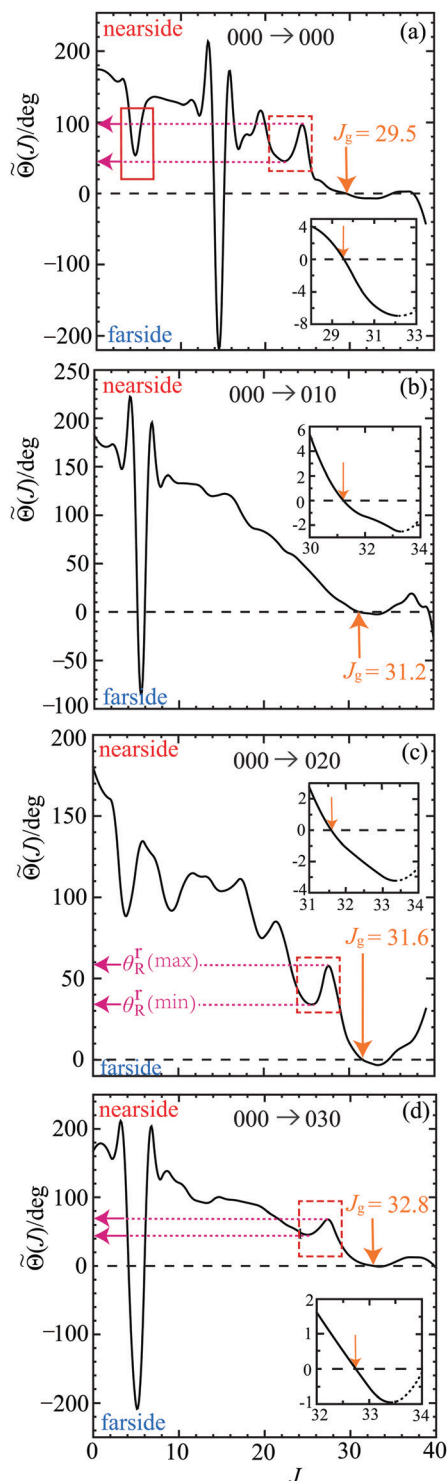
13354 | *Phys. Chem. Chem. Phys.*, 2021, **23**, 13349–13369

This journal is © the Owner Societies 2021

Fig. 4 Plots of the QDF, $\tilde{\Theta}(J)/\mathrm{deg}$, versus J, (black solid curve) at E_{trans} = 1.35 eV. An orange arrow indicates the value of the glory angular momentum variable, J_g, which satisfies $\tilde{\Theta}(J_g) = 0$. The inset shows the variation of $\tilde{\Theta}(J)/\mathrm{deg}$ close to $J = J_g$, where the black dotted curve indicates that the third branch of the QDF is not used in the SC glory analysis. The red solid rectangle encloses an example of a N rainbow (fold catastrophe) with a single minimum. The red dashed rectangles enclose two N rainbows with a minimum and a maximum, which together form part of a cusp catastrophe. The corresponding values of $\theta_R^r(\mathrm{min})$ and $\theta_R^r(\mathrm{max})$ are shown as pink dotted lines and pink arrows pointing toward the ordinate. The transitions are: (a) 000 → 000, (b) 000 → 010, (c) 000 → 020, (d) 000 → 030.

few J values, whereas a pronounced structure in a DCS, such as a rainbow, would typically involve a separation of many J values.

Contributions from these dips have been neglected in the following. We also note similar dips occur, and have been neglected, in the H + D$_2$ → HD + D reaction – see in particular Fig. 2b of ref. 23 and Fig. 8 of ref. 24.

● Next we examine the QDF for the 000 → 000 transition in more detail:

– At small J there is N rainbow (minimum) of the Airy type (or *fold catastrophe*[34]). For clarity, it is enclosed in a red solid rectangle in Fig. 4(a).

– At larger J, marked by a red dashed rectangle, there is another N rainbow (minimum) of Airy type. It is close to a maximum in the QDF, so this whole structure is part of a *cusp catastrophe*.[34]

– At even larger J, we have a forward glory, where $\tilde{\Theta}(J_g) = 0$. The behaviour of $\tilde{\Theta}(J)$ close to $J = J_g$ is shown in the inset.

● We observe, similar to the 000 case, rainbows and glories in the QDF plots for the 010, 020, 030 transitions in Fig. 4(b)–(d).

6. Theory of forward glory scattering

In this Section, we give the working equations for six forward glory theories; the derivations can be found elsewhere.[24–28]

6.1 Preliminaries

We begin by defining our notation in Fig. 5(a), which shows a plot of $\tilde{\Theta}(J)/\mathrm{deg}$ *versus* J in the glory region, $J = 28$ to $J = 33$, for the 000 → 000 transition. On inspection of Fig. 5(a), we note the following:

● The real root of $\tilde{\Theta}(J) = 0$ occurs at $J = J_g$.

● The real root of the first derivative, $\mathrm{d}\,\tilde{\Theta}(J)/\mathrm{d}\,J = 0$, occurs at $J = J_r(\mathrm{g})$, which defines the F rainbow angular momentum variable. The label "g" is added to indicate that $J_r(\mathrm{g})$ is close to J_g, and to distinguish it from other N rainbows present in the full QDF plot, which are written, J_r – an example of a N rainbow is shown in Fig. 5(b). Note that $\tilde{\Theta}(J_r(\mathrm{g})) = -\theta_R^r(\mathrm{g})$, with $\theta_R^r(\mathrm{g}) > 0$ being the rainbow angle. It provides a natural boundary for the applicability of some of the glory theories described in Section 6.2. Inspection of Fig. 1 shows that $|\tilde{S}(J)|$ is very small for $J > J_r(\mathrm{g})$, so contributions from this branch are neglected in our calculations.

● Semiclassically, $J < J_g$ corresponds to N scattering; in contrast, $J > J_g$ [with $J \le J_r(\mathrm{g})$] corresponds to F scattering.

● For $\tilde{\Theta}(J) = +\theta_R$, where $\theta_R \ge 0$, there is one *real* root, denoted $J = J_1 \equiv J_1(\theta_R)$, in the N scattering.

● For $\tilde{\Theta}(J) = -\theta_R$, where $0 \le \theta_R \le \theta_R^r(\mathrm{g})$ and $J \le J_r(\mathrm{g})$, there is one *real* root, denoted $J = J_2 \equiv J_2(\theta_R)$, in the F scattering.

● For $\tilde{\Theta}(J) = -\theta_R$, where $\theta_R > \theta_R^r(\mathrm{g})$, there are *no* real roots.

● For $\theta_R = 0$, J_1 and J_2 coalesce to J_g.

● In the SC analysis, it is convenient to define three branches for the QDF in Fig. 5(a) as follows:

branch 1: $28 \le J < J_g$ (nearside)
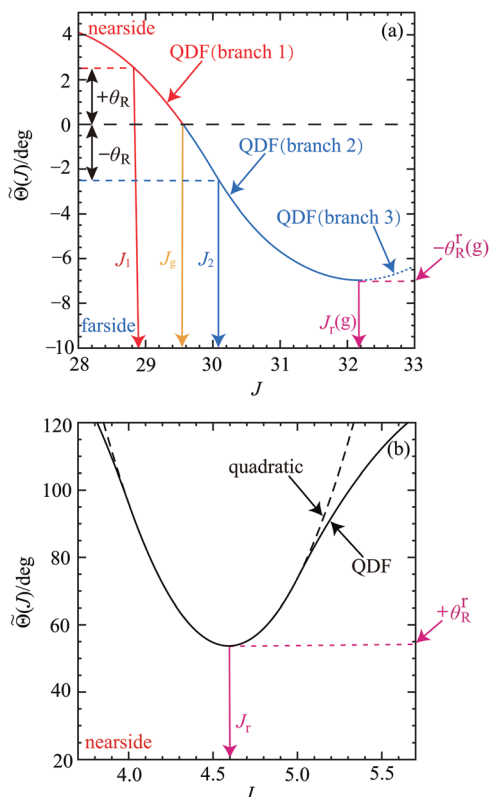branch 2: $J_g < J < J_r(\mathrm{g})$ (farside)

Fig. 5 Plots for the 000 → 000 transition of Fig. 4(a) at E_{trans} = 1.35 eV giving the notations used in the SC glory and rainbow theories for all four transitions. (a) $\tilde{\Theta}(J)/\text{deg}$ *versus* J close to $J = J_g$ for the range $J = 28$ to $J = 33$. The three branches of the QDF used in the SC analysis are indicated: branch 1 (nearside, red solid curve), branch 2 (farside, blue solid curve) and branch 3 (farside, blue dotted curve). The values of $\tilde{\Theta}(J)/\text{deg}$ at the angles $+\theta_R$ and $-\theta_R$ are indicated by a red dashed line (nearside) and a blue dashed line (farside) respectively. The corresponding values of the total angular momentum variable are denoted $J_1 \equiv J_1(\theta_R)$ (red solid arrow) and $J_2 \equiv J_2(\theta_R)$ (blue solid arrow) respectively. The orange arrow indicates J_g, which satisfies $\tilde{\Theta}(J_g) = 0$. The pink solid arrow shows the rainbow total angular momentum variable, $J_r(g)$, which is close to J_g. The corresponding rainbow value of $\tilde{\Theta}(J)/\text{deg}$ is denoted $-\theta_R^r(g)$ (pink dashed line). (b) $\tilde{\Theta}(J)/\text{deg}$ *versus* J for the range, $J = 3.7$ to $J = 5.7$. The pink solid arrow shows the rainbow total angular momentum variable, J_r. The corresponding nearside rainbow value of $\tilde{\Theta}(J)/\text{deg}$ is denoted $+\theta_R^r$ (pink dashed line). The black dashed curve shows the quadratic approximation to $\tilde{\Theta}(J)/\text{deg}$.

branch 3: $J_r(g) < J \leq 33$ (farside)

We also use the following notations, which follow from eqn (17):

$$\tilde{\Theta}'(J) \equiv \frac{d\tilde{\Theta}(J)}{dJ} = \frac{d^2 \arg \tilde{S}(J)}{dJ^2} \qquad (18)$$

and

$$\tilde{\Theta}''(J) \equiv \frac{d^2 \tilde{\Theta}(J)}{dJ^2} = \frac{d^3 \arg \tilde{S}(J)}{dJ^3} \qquad (19)$$

There are two SC N and F phases associated with J_1 and J_2, which are defined by[24–27]

$$\beta_1(\theta_R) \equiv \beta_1^{(-)}(\theta_R) = \arg \tilde{S}(J_1(\theta_R)) - \left[J_1(\theta_R) + \frac{1}{2} \right] \theta_R \qquad (20)$$

$$\beta_2(\theta_R) \equiv \beta_2^{(+)}(\theta_R) = \arg \tilde{S}(J_2(\theta_R)) + \left[J_2(\theta_R) + \frac{1}{2} \right] \theta_R \qquad (21)$$

There are also two "classical-like" N and F DCSs defined by[24–27]

$$\sigma_1(\theta_R) \equiv \sigma_1^{(-)}(\theta_R) = \frac{\left[J_1(\theta_R) + \frac{1}{2} \right] |\tilde{S}(J_1(\theta_R))|^2}{k^2 \sin \theta_R |\tilde{\Theta}'(J_1(\theta_R))|} \qquad (22)$$

$$\sigma_2(\theta_R) \equiv \sigma_2^{(+)}(\theta_R) = \frac{\left[J_2(\theta_R) + \frac{1}{2} \right] |\tilde{S}(J_2(\theta_R))|^2}{k^2 \sin \theta_R |\tilde{\Theta}'(J_2(\theta_R))|} \qquad (23)$$

Notice in eqn (20)–(23) we have employed the superscripts "−" and "+" for the SC nearside and farside scattering respectively. This is to avoid confusion with the superscripts "N" and "F" used in the PWS theories.

All the glory theories described below are derived from the following Poisson integral[24–27]

$$f_{\text{Poisson}}(\theta_R) = (2ik)^{-1} \int_{-1/2}^{\infty} dJ (2J+1) \tilde{S}(J) P_J(\cos \theta_R) \qquad (24)$$

Eqn (24) is obtained, as usual, by transforming the PWS into a Poisson series and then retaining the leading ($m = 0$) term.[24] Notice that $P_J(\bullet)$ is no longer a *Legendre polynomial* in eqn (24); rather it is a *Legendre function* (of the first kind). We have numerically evaluated eqn (24) for all four transitions and obtained very close agreement with the 000, 010, 020 PWS DCSs for $\theta_R \lesssim 100°$, and for $\theta_R \lesssim 50°$ for the 030 transition. These bounds include $\theta_R \leq 10°$ (or sometimes $\theta_R \leq 20°$), where the glory theories are applied.

6.2 Six semiclassical forward glory DCSs

We next list the working equations for the DCSs of six SC forward glory scattering theories.

6.2(a). Integral transitional approximation (ITA). Transitional approximations are valid for values of θ_R on, or close to, the axial caustic direction, $\theta_R = 0°$. The DCS for the ITA is[24–26]

$$\sigma_{\text{ITA}}(\theta_R) = \frac{1}{k^2} \left| \int_{-1/2}^{\infty} \tilde{S}(J) \left(J + \frac{1}{2} \right) dJ \right|^2 P_{J_g}(\cos \theta_R)^2 \qquad (25)$$

Notice in eqn (25), J_g is non-integral in general, so again $P_{J_g}(\cos \theta_R)$ is a Legendre function of the first kind. Also the ITA is exact for the Poisson integral (24) at $\theta_R = 0°$ because $P_{J_g}(\cos 0) = 1$.

In Section 8, we also need the ITA when the Hilb approximation is made for the Legendre function, namely[24–26]

$$P_J(\cos \theta_R) \sim \left(\frac{\theta_R}{\sin \theta_R} \right)^{1/2} J_0((J + 1/2)\theta_R) \qquad (26)$$

where $J_0(\bullet)$ is a Bessel function of order 0. The approximation (26) has an error $O(J^{-3/2})$ and is uniform for $\theta_R \in [0, \pi - \varepsilon]$ with $\varepsilon > 0$. We then write, ITA/J_0, when the Hilb approximation is applied to the ITA. For a numerical investigation of the validity of the Hilb formula and four other approximations for a Legendre function, see the Appendix of ref. 24.

13356 | *Phys. Chem. Chem. Phys.*, 2021, **23**, 13349–13369

This journal is © the Owner Societies 2021

6.2(b). Semiclassical transitional approximation (STA). The DCS for the STA is obtained when the integral in the ITA is evaluated by the stationary phase method.[24] It is given by

$$\sigma_{STA}(\theta_R) = \frac{2\pi\left(J_g + \frac{1}{2}\right)^2 |\tilde{S}(J_g)|^2}{k^2 |\tilde{\Theta}'(J_g)|} P_{J_g}(\cos\theta_R)^2 \tag{27}$$

In the limit $\theta_R \to 0°$, we have

$$\sigma_{STA}(\theta_R = 0) = \frac{2\pi\left(J_g + \frac{1}{2}\right)^2 |\tilde{S}(J_g)|^2}{k^2 |\tilde{\Theta}'(J_g)|} \tag{28}$$

6.2(c). Uniform Bessel asymptotic approximation (uBessel). The uBessel approximation allows for the coalescence of the stationary points J_1 and J_2 at $J = J_g$. It is given by

$$\sigma_{uBessel}(\theta_R) = \frac{\pi}{2}\varsigma(\theta_R)\left[\sigma_1(\theta_R)^{1/2} + \sigma_2(\theta_R)^{1/2}\right]^2 J_0(\varsigma(\theta_R))^2$$
$$+ \frac{\pi}{2}\varsigma(\theta_R)\left[\sigma_1(\theta_R)^{1/2} - \sigma_2(\theta_R)^{1/2}\right]^2 J_1(\varsigma(\theta_R))^2 \tag{29}$$

where $\varsigma(\theta_R)$ is defined by

$$\varsigma(\theta_R) = \frac{1}{2}[\beta_2(\theta_R) - \beta_1(\theta_R)] \tag{30}$$

In eqn (29), the $J_n(\bullet)$ are Bessel functions of order n [not to be confused with J_1 and J_2 in Fig. 5(a)]. The quantities $\beta_i(\theta_R)$ and $\sigma_i(\theta_R)$ for $i = 1, 2$ are given by eqn (20)–(23). The uBessel approximation can be used for $0 \le \theta_R < \theta_R^r(g)$. It diverges for $\theta_R \to \theta_R^r(g)$. Note that "uBessel" was called "USA" previously.[24–27]

6.2(d). Four Hankel asymptotic approximation (4Hankel). The 4Hankel approximation gets its name because it contains four Hankel functions, two of order 0 and two of order 1/3. It is a special case of the 6Hankel approximation,[27,28] which for a QDF of the shape in Fig. 5(a), is uniform in the DCS for both the glory scattering (around $J = J_g$) and the rainbow scattering [around $J = J_r(g)$]. Now, as previously mentioned in Section 6.1, the contribution from partial waves with $J > J_r(g)$ is very small, so the 6Hankel formula simplifies to the 4Hankel formula. It is given by[27,28]

$$\sigma_{4H}(\theta_R) = |f_{4H}^{(-)}(1|\theta_R) + f_{4H}^{(+)}(2|\theta_R)|^2 \tag{31}$$

where the first subamplitude is

$$f_{4H}^{(-)}(1|\theta_R) = \frac{1}{2ik}\left(\frac{\theta_R}{\sin\theta_R}\right)^{1/2}\frac{\pi}{3^{1/6}}\left[\frac{B_1(\theta_R)}{|\tilde{\Theta}''(J_1(\theta_R))|}\right]^{1/3}\left[J_1(\theta_R) + \frac{1}{2}\right]$$
$$\times |\tilde{S}(J_1(\theta_R))|\exp\{i[\arg\tilde{S}(J_1(\theta_R)) - B_1(\theta_R) + \pi/6]\}$$
$$\times H_0^{(2)}([J_1(\theta_R) + 1/2]\theta_R)H_{1/3}^{(1)}(B_1(\theta_R)) \tag{32}$$

with

$$B_1(\theta_R) = \frac{|\tilde{\Theta}'(J_1(\theta_R))|^3}{3[\tilde{\Theta}''(J_1(\theta_R))]^2} \tag{33}$$

Eqn (32) and (33) are valid for the N scattering where $\tilde{\Theta}(J_1) = +\theta_R > 0$.

On the farside, the second subamplitude is

$$f_{4H}^{(+)}(2|\theta_R) = \frac{1}{2ik}\left(\frac{\theta_R}{\sin\theta_R}\right)^{1/2}\frac{\pi}{3^{1/6}}\left[\frac{B_2(\theta_R)}{|\tilde{\Theta}''(J_2(\theta_R))|}\right]^{1/3}\left[J_2(\theta_R) + \frac{1}{2}\right]$$
$$\times |\tilde{S}(J_2(\theta_R))|\exp\{i[\arg\tilde{S}(J_2(\theta_R)) - B_2(\theta_R) + \pi/6]\}$$
$$\times H_0^{(1)}([J_2(\theta_R) + 1/2]\theta_R)H_{1/3}^{(1)}(B_2(\theta_R)) \tag{34}$$

with

$$B_2(\theta_R) = \frac{|\tilde{\Theta}'(J_2(\theta_R))|^3}{3[\tilde{\Theta}''(J_2(\theta_R))]^2} \tag{35}$$

The F subamplitude in eqn (34) and (35) is only valid on the bright side of the rainbow when the root of $\tilde{\Theta}(J) = -\theta_R$ is real. Thus in our calculations, we only apply the 4Hankel approximation (31) for $0 < \theta_R < \theta_R^r(g)$. It diverges for $\theta_R \to \theta_R^r(g)$.

6.2(e). Primitive semiclassical approximation (PSA). The PSA is obtained from the uBessel in eqn (29) when $\varsigma(\theta_R) \gg 1$.[24–27] This means we can replace the Bessel functions with their asymptotic approximations.[24–27] Alternatively, if the Hankel functions in eqn (31) are replaced by their asymptotic forms, we also obtain the PSA.[28] The result is

$$\sigma_{PSA}(\theta_R) = \sigma_2(\theta_R) + \sigma_1(\theta_R) + 2[\sigma_2(\theta_R)\sigma_1(\theta_R)]^{1/2}$$
$$\times \sin[\beta_2(\theta_R) - \beta_1(\theta_R)] \tag{36}$$

Eqn (36) can be applied for $0 < \theta_R < \theta_R^r(g)$ and is divergent as $\theta_R \to 0°$. The PSA has a NF physical interpolation similar to the interference pattern from the well-known "two slit experiment" – more details of this analogy are given in the Appendix of ref. 47.

6.2(f). Classical semiclassical approximation (CSA). The CSA is obtained by neglecting the sinusoidal term in the PSA of eqn (36). It averages over the glory oscillations and is useful because it describes the general trend in the scattering. It is given by

$$\left.\begin{aligned}\sigma_{CSA}(\theta_R) &= \sigma_2(\theta_R) + \sigma_1(\theta_R) \quad 0 < \theta_R < \theta_R^r(g) \\ &= \sigma_1(\theta_R) \quad \theta_R \ge \theta_R^r(g)\end{aligned}\right\} \tag{37}$$

Two special cases of the CSA are of interest – designated CSA/N and CSA/F – when we extract the N and F components from eqn (37) respectively. We have

$$\sigma_{CSA/N}(\theta_R) = \sigma_1(\theta_R) \quad \theta_R > 0$$

and

$$\sigma_{CSA/F}(\theta_R) = \sigma_2(\theta_R) \quad 0 < \theta_R < \theta_R^r(g)$$

The CSA, CSA/N and CSA/F all diverge as $\theta_R \to 0°$.

Some additional research on glories can be found in ref. 20–22 and 48–51.

7. Glory scattering results at forward angles

Fig. 6 and 7 show DCSs for the forward diffraction scattering in the range $\theta_R = 0°–10°$ for the four transitions. We are particularly concerned with the positions of the first minimum in the DCSs as they define the forward diffraction peaks. The following colour conventions are used for the DCSs in Fig. 6 and 7:

- Full PWS: black solid, with the label, PWS.
- tPWS: black dashed, with the label, PWS/J(25–33) for the window, $J = 25(1)33$. Likewise, PWS/J(28–35) and PWS/J(18–35).
- ITA and ITA/w: orange solid, with the label, ITA and ITA/w.
- STA: orange dashed, with the label, STA.
- 4Hankel: pink solid, with the label, 4Hankel.
- uBessel: green solid, with the label, uBessel.
- CSA: lilac dashed, with the label, CSA.
- CSA/N: red dotted, with the label, CSA/N.
- CSA/F: blue dotted, with the label, CSA/F.

We consider the 000 → 000 DCS in most detail, with less discussion for the 010, 030 cases, because they are similar to the 000 case. The 000 → 020 DCS exhibits some new features, which we analyse below.

7.1 DCSs for the 000 → 000 transition

The ITA and 4Hankel DCSs in Fig. 6 are seen to agree very well with the PWS DCS around its first minimum at $\theta_R \approx 5.0°$;

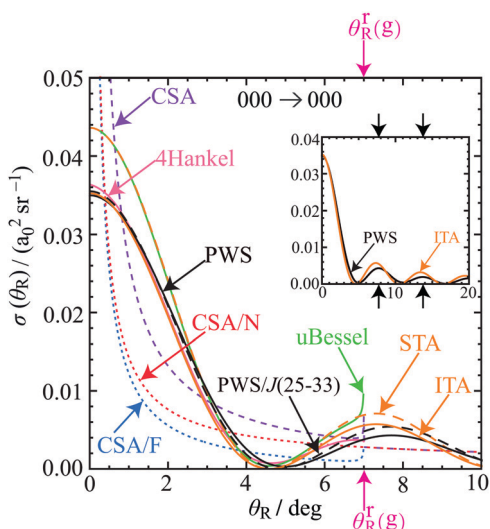**Fig. 7** Plots of $\sigma(\theta_R)$ versus θ_R at $E_{trans} = 1.35$ eV for the (a) 000 → 010, (b) 000 → 020, (c) 000 → 030, transitions for the angular range, $\theta_R = 0°$ to $\theta_R = 10°$. The DCSs plotted are: PWS (black solid curve), ITA (orange solid curve), STA (orange dashed curve), uBessel (green solid curve), 4Hankel (pink solid curve), CSA (lilac dashed curve). The pink rainbow angle in the glory region is denoted, $\theta_R^r(g)$; it forms the natural boundary for the uBessel, 4Hankel, and CSA/F approximations, which forms part of CSA. Also shown are DCSs, (black dashed curves) for restricted PWS for $J = 28–35$. In the inset for (b) there are also plotted DCSs for PWS/J(18–35) (black dotted curve) and the weighted ITA, denoted ITA/w (orange solid curve).

Fig. 6 Plots of $\sigma(\theta_R)$ versus θ_R at $E_{trans} = 1.35$ eV for the 000 → 000 transition for the angular range $\theta_R = 0°$ to $\theta_R = 10°$. The DCSs plotted are: PWS (black solid curve), PWS restricted to $J = 25–33$ (black dashed curve), ITA (orange solid curve), STA (orange dashed curve), uBessel (green solid curve), 4Hankel (pink solid curve). Also shown are the DCSs for CSA/F (blue dotted curve), CSA/N (red dotted curve) and their sum, CSA (lilac dashed curve). The pink rainbow angle in the glory region is denoted, $\theta_R^r(g)$; it forms the natural boundary for the uBessel, 4Hankel, and CSA/F approximations. The inset shows the ITA DCS and PWS DCS for the angular range $\theta_R = 0°$ to $\theta_R = 20°$, where the black arrows show the locations of two maxima, at $\theta_R = 7.71°$ and $\theta_R = 13.70°$, for the PWS DCS.

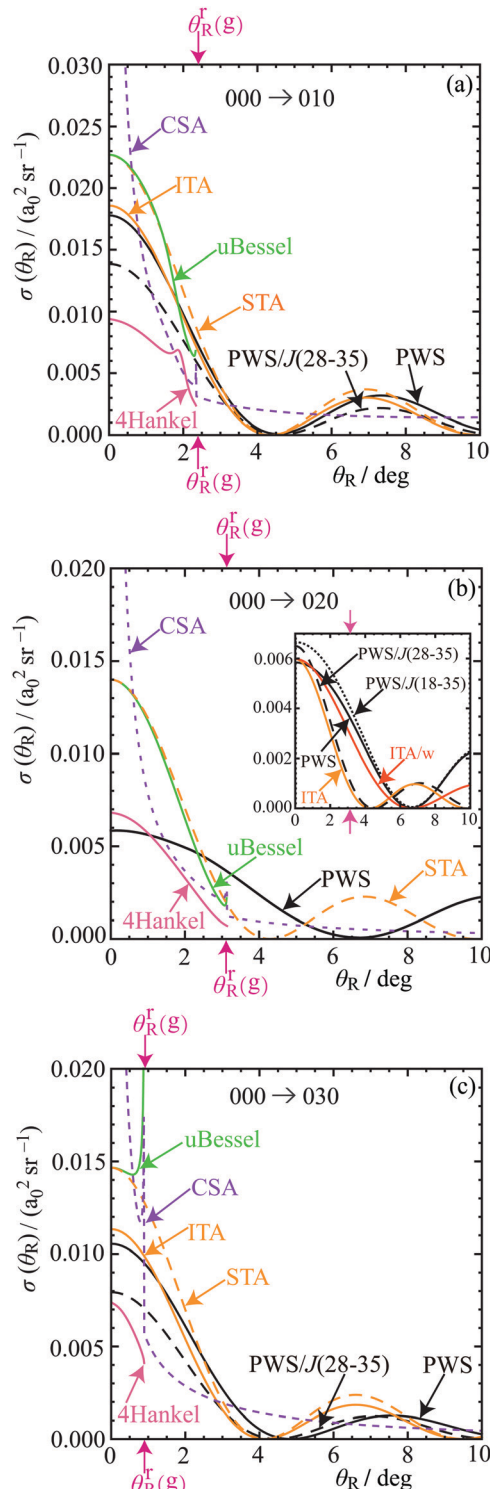**13358** | *Phys. Chem. Chem. Phys.*, 2021, **23**, 13349–13369

This journal is © the Owner Societies 2021

this is also the case for the STA and uBessel DCSs, as well as for the PSA DCS (not shown). As we then decrease θ_R, we find the ITA and 4Hankel DCSs remain in close agreement with the PWS DCS, in particular at $\theta_R = 0°$, although the STA and uBessel DCSs are somewhat larger. Notice the divergence of the 4Hankel, uBessel and CSA/F DCSs as $\theta_R \to \theta_R^r(g) \approx 7.0°$. The CSA, CSA/N and CSA/F DCSs are useful because they show the trend in the scattering by passing through the oscillations. For $\theta_R > 10°$, the ITA and STA DCSs drift out of phase relative to the PWS DCS, as expected. This is illustrated for the ITA DCS in the inset to Fig. 6 for $\theta_R \leq 20°$.

We also show in Fig. 6 the DCS for a window tPWS, namely one with partial waves, $J = 25(1)33$. We observe good agreement with the full PWS DCS, which suggests this window includes the important dynamics responsible for the forward scattering. Indeed this is the case, since we use $J_g = 29.5$, in the SC glory theories.

7.2 DCSs for the 000 → 010 and 000 → 030 transitions

The PWS and SC glory DCSs for the 010 and 030 cases are displayed in Fig. 7(a) and (c) respectively. Also shown are the DCSs for a tPWS with a window of $J = 28(1)35$. The trends in the SC and tPWS DCSs are seen to be similar to the 000 case in Fig. 6, and will not be discussed further. Note that the F rainbow angles for these two transitions are $\theta_R^r(g) \approx 2.3°$ and $\theta_R^r(g) \approx 0.9°$ respectively, which are both close to $\theta_R = 0°$. This means the range of applicability for the 4Hankel, uBessel and CSA/F approximations is very limited.

7.3 DCSs for the 000 → 020 transition

The 000 → 020 DCSs in Fig. 7(b) and its inset exhibit more complicated behaviour. The F rainbow angle occurs at $\theta_R^r(g) \approx 3.1°$, which again restricts the validity of the 4Hankel, uBessel and CSA/F approximations.

Next, we observe that the first minimum in the PWS DCS curve occurs at $\theta_R \approx 6.6°$, whereas the corresponding minimum for the ITA DCS curve is at $\theta_R \approx 4.3°$. These minima are clearly visible in the inset to Fig. 7(b). To understand this difference, we note that a tPWS DCS using the window $J = 28(1)35$ agrees closely with the ITA DCS. This suggests there may be other dynamical effects for $J \notin \{28,29,...,35\}$ contributing to the PWS DCS [or equivalently to the Poisson DCS of eqn (24)].

The inset shows a second tPWS DCS, which uses a wider window, $J = 18(1)35$. We now observe much better agreement with the full PWS DCS, in particular around its minimum at $\theta_R \approx 6.6°$. Furthermore, inspection of the QDF in Fig. 4(c) shows there are two minima and two maxima (*i.e.*, four Airy N rainbows), for the J-range starting at $J = 18$ and ending at $J = 35$. Semiclassically, this whole structure of four extrema corresponds to a *swallowtail catastrophe*.[52] We expect there may be a contribution from the dark side of the deeper rainbow with a minimum near $J \approx 25.6$. We will show that this is the case in Section 11, where we find there is a hidden rainbow present in the DCS for the angular range, $\theta_R \approx 10°-60°$.

The discussion just given implies there are one (or more) contributions to the Poisson integral (24) in addition to J values close to $J = J_g$. A straightforward way to improve the ITA is to multiply J_g by a weighting factor, w, to obtain an effective J_g-value, denoted J_{wg}, *i.e.*, $J_{wg} = wJ_g$. We call this *weighted approximation*, ITA/w. With the choice, $w = 0.64$, we find, $J_{wg} = 20.2$. The inset shows the resulting ITA/w DCS, as well as the tPWS DCS with the window, $J = 18(1)35$, and we now observe much better agreement for these two DCSs with the full PWS DCS, especially around the minimum at $\theta_R \approx 6.6°$. Notice that $J_{wg} = 20.2$ is contained within the real interval, $[18,35]$.

7.4 Conclusions

We have applied six SC glory theories, as well as tPWS, to the forward angle scattering for all four transitions. For the 000, 010, 030 cases, the ITA DCSs agree closely with the PWS DCSs, showing that the pronounced forward peak is indeed mainly a glory. The 000 case is the most favourable to analyse because it has the largest F rainbow angle of $\theta_R^r(g) \approx 7.0°$. Smaller rainbow angles limit the applicability of the uBessel, 4Hankel and CSA/F approximations. The DCS for the 000 → 020 transition is more complicated. But our analysis showed that other dynamical effects are contributing to the scattering for the 020 case, in addition to the SC glory contribution.

8. Theory of corona diffraction: tests for glory and corona small-angle scattering

Yuan *et al.* have suggested[5] that the oscillatory small-angle scattering for the product DCSs of the H + HD reaction be called *coronae*, because of their *qualitative* resemblance to atmospheric coronae.[29–33] Yuan *et al.* write "it is reasonable to make the analogy between the two phenomena" (ref. 5, Supplementary Information, p. 17). Here we *quantitatively* explore the similarities and differences between corona and glory small-angle scattering.

An atmospheric corona is sometimes seen as a series of coloured concentric rings around the sun or moon, when they are partially covered by a thin mist or cloud.[29–33] An atmospheric corona should not be confused with a solar (or stellar) corona, a coronavirus or a Corona beer.

Glories and coronae have some similarities in their small-angle scattering, as will be illustrated below. However, they are physically and mathematically distinct phenomena. We next present two small-angle *ratio* tests, which we collectively call "CoroGlo". We then apply CoroGlo to the four PWS DCSs, thereby letting us distinguish between the presence of a glory or a corona in the forward scattering. The tests are adapted from results described by Canto and Hussein.[53]

8.1 CoroGlo test for a forward small-angle corona

A corona is usually modelled as Fraunhofer diffraction from a hard (impenetrable, rigid) sphere. In the SC limit, for a sphere of radius a, the DCS is given by[29–33,53–59]

$$\sigma_C(\theta_R) = \frac{1}{4}a^2 \cot^2(\theta_R/2)J_1(ka\sin\theta_R)^2$$
$$= \left[ka^2\frac{(1+\cos\theta_R)}{2}\frac{J_1(ka\sin\theta_R)}{ka\sin\theta_R}\right]^2 \quad (38)$$

This journal is © the Owner Societies 2021

Phys. Chem. Chem. Phys., 2021, **23**, 13349–13369 | **13359**

In our applications, we have $\theta_R \lesssim 10°$, so it is a very good approximation to replace $(1 + \cos\theta_R)/2$ by 1 in eqn (38), yielding

$$\sigma_C(\theta_R) \approx \frac{k^2 a^4}{4} \left[\frac{2J_1(x)}{x}\right]^2 \quad x = ka\sin\theta_R \qquad (39)$$

In optics, the quantity $[2J_1(x)/x]^2$ is called the *Airy diffraction pattern*.[53–59] Here we call it the *corona diffraction pattern* (CDP) to avoid confusion with Airy's theory of the rainbow discussed in Sections 10 and 11. Next, we note that $[2J_1(x)/x]^2 \to 1$ as $x \to 0$, so we can write eqn (39) in the form

$$\sigma_C(\theta_R) \approx \left[\frac{2J_1(x)}{x}\right]^2 \sigma_C(\theta_R = 0) \quad x = ka\sin\theta_R \qquad (40)$$

Eqn (40) shows that $\sigma_C(\theta_R)$ is a universal function of x, multiplied by a scaling factor, and so we can also write, $\sigma_C(x)$. Fig. 8 shows a graph of the CDP, drawn as a black solid curve, for the range $x = 0$–10; we see a pronounced forward peak accompanied by weak subsidiary oscillations.

A corona can be characterized by the *ratio* of its primary maximum at $x = 0$ (or $\theta_R = 0$) to the maxima of its subsidiary oscillations (ref. 53, p. 310) and in particular the adjacent maximum. We denote the locations of the maxima by x_i with $i = 0, 1, 2, \ldots$ Thus, $x_{i=0} = 0$ and $x_{i=1} = 5.14$ – see Fig. 8. The corresponding values of the DCS are $\sigma_C(x = x_{i=0} = 0)$ and $\sigma_C(x = x_{i=1} = 5.14)$. Then the *corona diffraction ratio* (CDR) is defined as

$$R_C \equiv R_C(\max 0/\max 1) = \frac{\sigma_C(x_{i=0})}{\sigma_C(x_{i=1})}$$

$$\approx \left[\frac{x_1}{2J_1(x_1)}\right]^2 \qquad (41)$$

$$\approx 57.1$$

Thus, if we measure the *ratio* of the primary maximum to the adjacent maximum for a PWS DCS and obtain a value
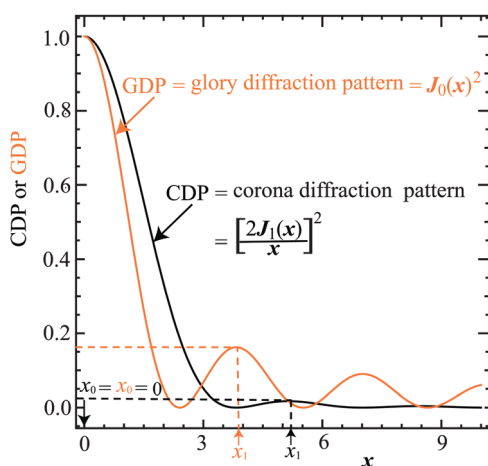

Fig. 8 Plots of the CDP = corona diffraction pattern = $[2J_1(x)/x]^2$, (black solid curve) and the GDP = glory diffraction pattern = $J_0(x)^2$, (orange solid curve), *versus* x. The position of the principal maximum for both curves is at $x_0 = 0$. The positions of the adjacent maxima for the CDP and GDP curves occur at $x_1 = 5.14$ (black arrow) and 3.83 (orange arrow) respectively.

close to 57, this tells us that a corona is dominating the forward small-angle scattering. Note in ref. 53, p. 310, the CDR is called the "forward concentration parameter".

In passing, we note that a straightforward method for finding the position, x_1, of the $i = 1$ maximum in eqn (40) and (41) is to numerically solve $d[2J_1(x)/x]^2/dx = 0$. An alternative, simpler, method is to use the differential recurrence relation[60]

$$\frac{d}{dx}\left[\frac{J_n(x)}{x^n}\right] = -\frac{J_{n+1}(x)}{x^n} \quad n = 0, 1, 2, \ldots$$

for $n = 1$. Then the position of the $i = 1$ maximum is a root of $J_2(x) = 0$.

8.2 CoroGlo test for a forward small-angle glory

Next we derive a *ratio* test for a forward glory (ref. 53, p. 241) which we denote, $R_G \equiv R_G(\max 0/\max 1)$, analogous to the corona ratio test, $R_C \equiv R_C(\max 0/\max 1)$, of eqn (41). To do this, we employ the ITA/J_0 approximation of eqn (25) and (26), in which the Legendre function is approximated by a Bessel function of order zero using the Hilb formula. In addition, since $\theta_R \lesssim 10°$, we can replace $\theta_R/\sin\theta_R$ by 1 to a very good approximation. We get

$$\sigma_G(\theta_R) \approx \frac{1}{k^2}\left|\int_{-1/2}^{\infty} \tilde{S}(J)\left(J + \frac{1}{2}\right)dJ\right|^2 J_0(x)^2 \quad x = \left(J_g + \frac{1}{2}\right)\theta_R$$

Since, $J_0(0) = 1$, we can also write

$$\sigma_G(\theta_R) \approx J_0(x)^2 \sigma_G(\theta_R = 0) \quad x = \left(J_g + \frac{1}{2}\right)\theta_R \qquad (42)$$

Eqn (42) shows that $\sigma_G(\theta_R)$ is a universal function of x, multiplied by a scaling factor; we can also write $\sigma_G(x)$. We call $J_0(x)^2$, the *glory diffraction pattern* (GDP). A graph of the GDP, drawn as an orange solid curve, for x in the range 0–10 is shown in Fig. 8. We see there is a forward diffraction peak, accompanied by subsidiary oscillations. An important observation is that the oscillations for the GDP are much more pronounced than those for the CDP.

The oscillations for both the CDP and the GDP arise from nearside–farside interference. This follows from the large x asymptotic approximation[61]

$$J_n(x) \sim \left(\frac{2}{\pi x}\right)^{1/2}\cos\left(x - \frac{\pi}{2}n - \frac{\pi}{4}\right) \quad n = 0, 1, 2, \ldots$$

when the cosine is decomposed into complex exponentials.

Similar to the corona case, we can characterize a glory by the *ratio* of its primary maximum at $x = 0$ (or $\theta_R = 0°$) in the GDP to the maxima of its subsidiary oscillations, and in particular the adjacent maximum (ref. 53, p. 241). We denote the locations of the maxima of $J_0(x)^2$ by x_j with $j = 0, 1, 2, \ldots$ Thus $x_{j=0} = 0$ and $x_{j=1} = 3.83$ – see Fig. 8. The corresponding values of the DCS are

13360 | *Phys. Chem. Chem. Phys.*, 2021, **23**, 13349–13369

This journal is © the Owner Societies 2021

then $\sigma_G(x = x_{j=0} = 0)$ and $\sigma_G(x = x_{j=1} = 3.83)$. Next, we define the *glory diffraction ratio* (GDR) by

$$R_G \equiv R_G(\max 0/\max 1) = \frac{\sigma_G(x_{j=0})}{\sigma_G(x_{j=1})}$$

$$\approx \left[\frac{1}{J_0(x_1)}\right]^2 \tag{43}$$

$$\approx 6.2$$

Thus, if we measure the *ratio* of the primary maximum to the adjacent maximum for a PWS DCS and obtain a value close to 6, this tells us that a glory is dominating the forward small-angle scattering.

8.3 Application of the CoroGlo corona and glory tests to PWS DCSs

In this section, we apply the CoroGlo corona and glory tests of eqn (41) and (43) respectively, to the PWS DCSs displayed in Fig. 3 for $\theta_R = 0°–180°$, or in more detail in Fig. 6 and 7 for a smaller range of angles. We recall that the PWS DCSs have been calculated using accurate quantum S matrix elements and are in close agreement with the experimental results. We write R_Q for the *ratio* of the forward diffraction peak to the adjacent maximum for the accurate quantum PWS DCSs. We obtain the following ratios:

$$000 \to 000: R_Q = 8.1,$$

$$000 \to 010: R_Q = 5.6,$$

$$000 \to 020: R_Q = 2.6,$$

$$000 \to 030: R_Q = 8.3.$$

If we compare the R_Q values with the CDR value of 57.1, we see they are quite different. This implies corona scattering *makes a minor contribution* to the small-angle DCSs.

The R_Q values for the 000, 010, and 030 cases are much closer to the GDR value of 6.2, which tells us that glory scattering *makes a major contribution* to the small-angle region for these cases. The results from this test are consistent with the SC glory analyses of Sections 6 and 7. Since the R_Q values are not very close to 6.2, this implies (as expected) there are small contributions from other mechanisms.

The largest deviation from $R_G = 6.2$ occurs for the 020 case, which suggests there is another, more significant, contribution to the small-angle scattering, in addition to the glory mechanism. This is consistent with the SC glory analysis of the PWS DCS in Fig. 7(b). In Sections 10 and 11, we will show that there is indeed a contribution from a hidden rainbow to the 020 PWS DCS.

9. Periods of the oscillations in the small-angle PWS DCSs

In Section 8.3, we showed that the height of the primary maximum in a DCS (located at $\theta_R = 0°$) and the height of its

adjacent maximum provided valuable information on the dynamics of the reaction *via* the CoroGlo tests. Now upon examination of Fig. 3, or in more detail in Fig. 6, 7 and 9, we see that the periods of the NF oscillations are approximately constant, usually in the range, 6°–7°. We next show how to obtain dynamical information from this observation.

According to eqn (25), the dependence of the ITA DCS on θ_R is given by the square of the Legendre function, namely $P_{J_g}(\cos\theta_R)^2$.
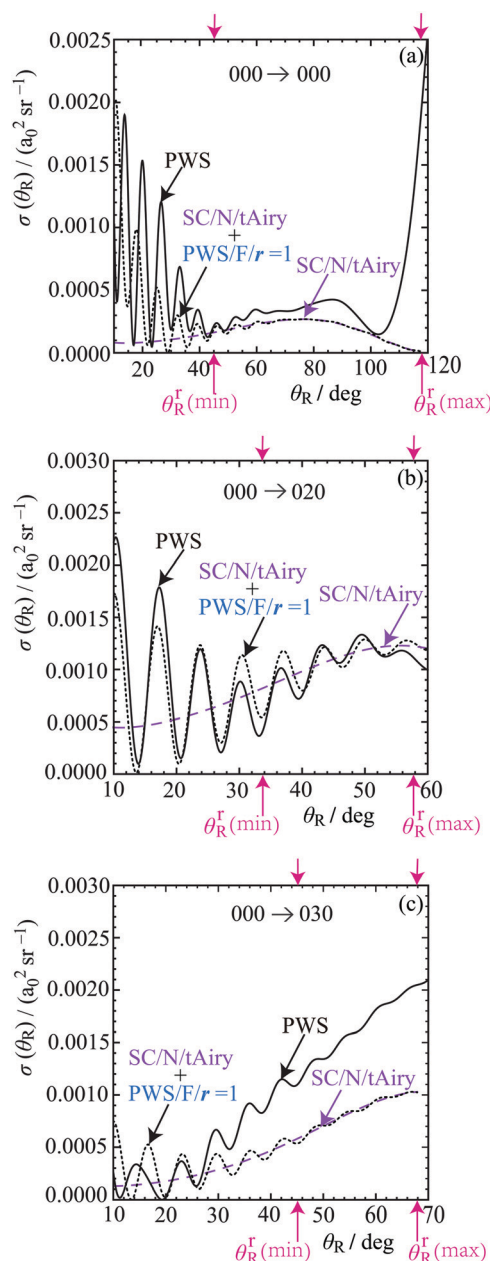

Fig. 9 Plots of $\sigma(\theta_R)$ *versus* θ_R at $E_{trans} = 1.35$ eV. The DCSs plotted are: PWS (black solid curve), SC/N/tAiry (lilac dashed curve), SC/N/tAiry + PWS/F/r = 1 (black dotted curve). The pink arrows mark the locations of the rainbow angles, $\theta_R^r(\min)$ and $\theta_R^r(\max)$, which are also shown in Fig. 4. The transitions are: (a) 000 → 000 for $\theta_R = 10°$ to $\theta_R = 120°$, (b) 000 → 020 for $\theta_R = 10°$ to $\theta_R = 60°$, (c) 000 → 030 for $\theta_R = 10°$ to $\theta_R = 70°$.

This journal is © the Owner Societies 2021

Phys. Chem. Chem. Phys., 2021, **23**, 13349–13369 | **13361**

This is also the case for the STA of eqn (27). Now for $J_g \sin \theta_R \gg 1$, we can use the asymptotic approximation[62]

$$P_{J_g}(\cos \theta_R) \sim \left[\frac{2}{\pi(J_g + 1/2)\sin \theta_R}\right]^{1/2} \cos\left[\left(J_g + \frac{1}{2}\right)\theta_R - \frac{\pi}{4}\right] \tag{44}$$

For example, if $J_g = 29.5$, then eqn (44) is a good approximation for $\theta_R \gtrsim 2°$. With the help of eqn (44), we find the period of the ITA oscillations is given by the simple formula

$$\Delta \theta_R / \text{rad} = \frac{\pi}{J_g + 1/2} \tag{45}$$

which is an example of eqn (16).

We consider the $000 \rightarrow 000$ transition first. The inset to Fig. 6 shows that the ITA DCS closely follows the PWS DCS out to $\theta_R = 20°$. The PWS DCS has maxima at $\theta_R = 7.71°$ and $\theta_R = 13.70°$, so the period is, $\Delta\theta_R/\text{deg} = 5.99$. From eqn (45), we obtain $J_g = 29.6$, which is very close to the value $J_g = 29.5$ given by the maximum of the $\arg\tilde{S}(J)/\text{rad}$ versus J graph in Fig. 2(a).

We next repeat the procedure just described for the 010, 020, 030 PWS DCSs. We obtain estimates for J_g of 28.6, 25.5, 26.0, which can be compared with the values 31.2, 31.6 (or 20.2 for ITA/w), 32.8 used in the ITA analysis respectively. The errors are now larger, being within 8–26% of the ITA values, which can be understood because the ITA DCSs become increasingly out-of-phase relative to the PWS DCSs, as θ_R increases beyond $10°$. Nevertheless, these estimates are still useful given the simplicity of eqn (45).

10. Theory of nearside rainbow scattering

Inspection of the QDFs in Fig. 4 reveals the existence of many extrema, which correspond to Airy rainbows in the SC theory.[52] The question then arises: are these rainbows also visible in the DCSs? Looking at Fig. 3, there are no obvious "pronounced" primary rainbows (plus supernumerary rainbows) of Airy type in the DCSs, similar to those found in elastic scattering.[4,63] Note: it is now known that such pronounced primary rainbows plus their supernumeraries can indeed occur in the DCSs of state-to-state chemical reactions.[64,65]

However there is another possibility. It has been proven using rigorous asymptotic techniques that "broad" F Airy rainbows can occur in state-to-state reactive DCSs. These broad rainbows have been found in the DCSs of the $F + H_2 \rightarrow FH(\nu_f = 3) + H$ reaction,[27,66] both in simulations of the 1985 experiment of Neumark et al.,[67] as well as in the more recent 2008 experiment of Wang et al.[68] Broad Airy rainbows are also called "hidden",[64,65] because their appearance in a DCS is quite different from that of pronounced Airy rainbows. Indeed, it took 24 years[66] before it was realized that the experimental DCSs of Neumark et al.[67] contain a hidden rainbow. It is also important to stress that the hidden rainbows in the $F + H_2$ reaction are F rainbows, whereas the rainbows in Fig. 4, which we discuss next, are N rainbows.

In the next two subsections, we have chosen four N rainbows in Fig. 4(a), (c) and (d) for further SC analysis for the 000, 020,

030 cases respectively, [two rainbows are in Fig. 4(a)]. The QDF curve for the $000 \rightarrow 010$ transition in Fig. 4(b) only possesses slight undulations with no prominent extrema, so we do not consider this case.

10.1 A single N rainbow in the QDF at small J

Inspection of Fig. 4(a) for the $000 \rightarrow 000$ transition shows there is a minimum in the QDF at small J, namely from $J \approx 3.7$ to $J \approx 5.7$. Including the dark (classically forbidden) side of the rainbow, the corresponding range for $\tilde{\Theta}(J)$ is from $\tilde{\Theta} \approx 20°$ to $\tilde{\Theta} \approx 120°$. This $(J, \tilde{\Theta}(J))$ rainbow region is enclosed by a red *solid* rectangle in Fig. 4(a) and is drawn in more detail in Fig. 5(b). We denote the rainbow angular momentum variable where $d\tilde{\Theta}(J)/dJ = 0$ by J_r and the corresponding rainbow angle by θ_R^r, thus, $\tilde{\Theta}(J_r) = +\theta_R^r$.

There are two standard (although related) methods[34] for calculating the SC N subamplitude for a QDF rainbow of the type shown in Fig. 5(b):

(a) The *uniform semiclassical Airy* approximation.[34] In a systematic notation, this is denoted SC/N/uAiry, or uAiry for short. Now the uAiry approximation is straightforward to apply on the bright side of the rainbow, *i.e.*, for $\theta_R > \theta_R^r$, but not on its the dark side, *i.e.*, for $\theta_R < \theta_R^r$, because the roots of the stationary phase equation, $\tilde{\Theta}(J) = +\theta_R$, are then complex valued – a situation which is awkward to handle for numerical input S matrix data.

If we replace the Airy functions in the uAiry approximation by their asymptotic forms, we obtain the *primitive semiclassical approximation*.[34] We denote this by PSA/NN because it contains two N sub-subamplitudes and to avoid confusion with the PSA ($\equiv$ PSA/NF) that arises in the theory of glory scattering given in Section 6.2(e). Dropping the interference term in PSA/NN gives the *classical semiclassical approximation*, CSA/NN.

(b) The *transitional semiclassical Airy* approximation.[34] In a systematic notation, this is denoted SC/N/tAiry, or tAiry for short. The tAiry makes a quadratic approximation for $\tilde{\Theta}(J)$ about $J = J_r$, and Fig. 5(b) show this is accurate up to $\tilde{\Theta} \approx 90°$. The tAiry approximation has the advantage that it can be applied on both the bright and dark sides of the rainbow, since it only depends on quantities defined at (J_r, θ_R^r). Because we will be showing DCSs using the tAiry approximation in Section 11, we write down the N subamplitude here:

$$f_{\text{tAiry}}^{(-)}(\theta_R) = \frac{1}{k}\left[\frac{2\pi(J_r + 1/2)}{\sin \theta_R}\right]^{1/2} \left|\tilde{S}(J_r)\right|$$

$$\times \frac{\exp\{i[\arg \tilde{S}(J_r) - (J_r + 1/2)\theta_R - \pi/4]\}}{q_r^{1/3}} \tag{46}$$

$$\times \text{Ai}\left(\frac{\theta_R^r - \theta_R}{q_r^{1/3}}\right)$$

where

$$q_r = \frac{1}{2}\frac{d^2\tilde{\Theta}(J)}{dJ^2}\bigg|_{J=J_r} \tag{47}$$

13362 | *Phys. Chem. Chem. Phys.*, 2021, **23**, 13349–13369

This journal is © the Owner Societies 2021

The corresponding tAiry DCS is given by

$$\sigma_{tAiry}^{(-)}(\theta_R) = |f_{tAiry}^{(-)}(\theta_R)|^2 \qquad (48)$$

Additional remarks:

(a) The N LAM for the tAiry approximation (46), denoted $LAM_{tAiry}^{(-)}(\theta_R)$, is approximately equal to $-(J_r + 1/2)$, which is independent of θ_R.[16,27]

(b) The tAiry and uAiry approximations become equivalent for a quadratic QDF provided the pre-exponential factor is a constant in the original SC integral.[34] For a numerical illustration, see example 1 in the Appendix of ref. 28.

(c) The tAiry approximation has also been applied in examples 2 and 3 of the Appendix of ref. 28 to two oscillating integrals of relevance to molecular scattering, namely a real-valued *oddoid integral* of order two and a complex-valued *swallowtail integral*.[52] For both of these integrals, the tAiry approximation is in very good agreement with the exact numerical values in the dark regions.

(d) We can make a check on eqn (46) and (47) by putting $|\tilde{S}(J_r)| \to 1$ and $\arg\tilde{S}(J_r) \to 2\delta(J_r)$; we then obtain a tAiry result that is equivalent to one arising in the SC theory of elastic cusped rainbows using the *Pearcey integral* [see eqn (3.40) and (3.41) of ref. 69].

10.2 Three N rainbows in the QDF at large J

Fig. 4 shows there are three N rainbows at large J which are indicated by red *dashed* rectangles. Their shapes on the inside-left of a rectangle are similar to the rainbow in Section 10.1 and Fig. 5(b), being approximately quadratic. The corresponding rainbow angle for this case is denoted, $\theta_R^r(min)$. On the inside-right of the dashed rectangles, the QDFs bend over and there is a maximum. We denote the corresponding rainbow angle by $\theta_R^r(max)$. The values of $\theta_R^r(min)$ and $\theta_R^r(max)$ are marked by pink arrows and dotted pink lines pointing towards the ordinates in Fig. 4.

Having identified four N rainbows in the QDFs, we next carry out a SC analysis in the following section to see if these rainbows make an important contribution to the DCSs.

11. Nearside rainbow angular scattering results

We consider the four rainbows in the QDFs at small J and large J separately.

11.1 Nearside rainbow scattering at small J

Firstly, we consider the N rainbow at small J in Fig. 4(a) for the $000 \to 000$ transition; it is enclosed by a red solid rectangle. Our main SC tool is the tAiry subamplitude of eqn (46) and (47). We find that the corresponding tAiry DCS of eqn (48) is very small. As a check, we have also applied the uAiry, PSA/NN, and CSA/NN approximations in the range, $\theta_R > \theta_R^r$, and obtained the same result, *i.e.*, there is no hidden rainbow present in the DCS. These findings also tell us that the widely-spaced oscillations for $\theta_R \gtrsim 90°$ in Fig. 3(a) are not a S matrix phase

interference effect. Rather, in Section 13 we will use the SOM to show that these oscillations arise from the variation of $|\tilde{S}(J)|$ with J.

11.2 Nearside rainbow scattering at large J

Secondly, we consider the three N rainbows at large J in Fig. 4(a), (c) and (d) for the 000, 020, 030 cases respectively; they are enclosed by red dashed rectangles. Since we require results for $\theta_R < \theta_R^r(min)$, our main tool is again the tAiry approximation, although we have also used the uAiry, PSA/NN, and CSA/NN approximations for $\theta_R > \theta_R^r(min)$.

Our results for the DCSs are plotted in Fig. 9. Notice that the abscissae start at $\theta_R = 10°$, in order to overlap with Fig. 6 and 7, and end just beyond the $\theta_R = \theta_R^r(max)$ values. This is because the SC approximations we employ are not valid for $\theta_R \gtrsim \theta_R^r(max)$. Now the $000 \to 020$ transition has the smallest value of $\theta_R^r(min)$ and no nearby additional rainbows, so we discuss the SC DCSs for this transition first.

Inspection of Fig. 9(b) shows that, $\sigma_{tAiry}^{(-)}(\theta_R)$, which is also labelled SC/N/tAiry and drawn as a lilac dashed curve, passes through the oscillations in the full PWS DCS. Next, we have added to the tAiry subamplitude, the contribution from the F $r = 1$ PWS subamplitude, which is also labelled PWS/F/$r = 1$. The resulting total DCS

$$\sigma_{tAiry}^{(F,r=1)}(\theta_R) = |f_{tAiry}^{(-)}(\theta_R) + f_{r=1}^{(F)}(\theta_R)|^2 \qquad (49)$$

which is drawn as a black dotted curve in Fig. 9(b). We see there is good agreement with the full PWS DCS, in particular for the positions and periods of the oscillations, which is a delicate test for a SC theory. The good agreement also holds in the dark region, where $\theta_R < \theta_R^r(min) \approx 33.8°$. Thus we conclude that the DCS for the $000 \to 020$ transition contains a broad, or hidden, N rainbow in the angular region from $\theta_R = 10°$ to approximately, $\theta_R = \theta_R^r(max) \approx 57.7°$. We note that this is an example of Fraunhofer scattering (see ref. 27 for another example). Also, if the F $r = 1$ subamplitude is replaced by the F $r = 0$ subamplitude in eqn (49), we obtain essentially the same total DCS.

We can make another check on this rainbow. The PWS N LAM(θ_R) for $r = 1$, denoted $LAM_{r=1}^{(N)}(\theta_R)$, varies slowly in the range $\theta_R = 10°-60°$, with a mean value of -26.2. For a N rainbow, we then expect the following relations to hold:[16,27]

$$|\langle LAM_{r=1}^{(N)}(\theta_R)\rangle| \approx |LAM_{tAiry}^{(-)}(\theta_R)| \approx J_r + 1/2 \approx ReJ_0 + 1/2 \qquad (50)$$

where $\langle \ldots \rangle$ denotes a mean value, and J_0 is the position of the leading Regge pole in the complex angular momentum (CAM) plane. We have used *Thiele rational interpolation*[27] to determine J_0, and obtained the value, $J_0 = 25.7 + 3.1i$ (after removal of Froissart doublets), using as input data, $\{\tilde{S}_J\}$, in the range $J = 10(1)33$. Since, $J_r = 25.4$, we see that the approximations (50) are satisfied. This tells us that the PWS, SC and CAM theories are consistent in their descriptions of the angular scattering.

The rainbow scattering in Fig. 9(b) continues into the region, $\theta_R < 10°$, thereby also making a contribution at small forward angles. In particular, it agrees well with the PWS DCS down to $\theta_R \approx 2.5°$. An additional mechanism was suggested by

Paper

our SC glory analysis in Section 7.3, but not identified. Now we see a broad rainbow also contributes at small angles and is the unidentified mechanism.

Next we consider the DCSs for the 000 → 030 transition in Fig. 9(c). We see similar rainbow behaviour to the 020 case, but restricted to $20° \lesssim \theta_R \lesssim 30°$. We can understand this result from Fig. 4(d), which shows that the QDF minimum and maximum in the red dashed rectangle are rather close to each other, their angular separation being about $23°$. This suggests a full SC analysis may require the uniform Pearcey asymptotic approximation;[69] however this is beyond the scope of the present paper.

Finally, we examine the DCSs for the 000 → 000 transition in Fig. 9(a). This is similar to the 030 case in that the rainbow is confined to a small angular region, namely $30° \lesssim \theta_R \lesssim 50°$. Fig. 4(a) shows the presence of additional rainbows just outside the red dashed rectangle to its left, which will probably make an additional contribution to the tAiry subamplitude for $\theta_R \gtrsim 50°$.

Some additional research on rainbows can be found in ref. 49, 53, 56–59 and 70–75.

11.3 Conclusions

This is the first report of N rainbows in the DCSs of state-to-state chemical reactions. The 020 case exhibited a broad or hidden rainbow over the angular range, $2.5° \lesssim \theta_R \lesssim 60°$. The 000 and 030 cases also showed hidden rainbow behaviour, but over a smaller range of angles.

12. Semiclassical optical model (SOM): theory

The SOM is a simple procedure for calculating the DCSs of state-to-state chemical reactions. It was introduced by Herschbach[35,36] and has subsequently been applied to several reactions.[12,76–87] In addition, the SOM has been generalized to a "sticky optical model" for reactions which involve formation of a long-lived complex.[47] In the NF terminology of Section 2, the SOM is an example of an (approximate) N theory. It is also a limiting case of the complex angular momentum (CAM) theory developed in ref. 47 for reactive angular scattering.

Unlike the glory analysis of Section 6 – or the rainbow analysis of Section 10 – the SOM does not use the phase of each S matrix element, rather it employs just the moduli, $|\tilde{S}_J|$, or more precisely the corresponding *reaction probability*, defined by

$$P_J \equiv |\tilde{S}_J|^2 \quad J = 0,1,2,\ldots \tag{51}$$

The SOM makes two assumptions:

Assumption 1. The reaction can be represented by the *classical* collision of two hard spheres. The classical DCS for a hard sphere collision is isotropic, being given by:

$$\sigma_{hs}(\theta_R) = (d/2)^2 \tag{52}$$

where d is the sum of the radii of the two hard spheres representing the reactants (or equivalently the average diameter of the spheres). This result assumes that the reaction is direct

with specular collision dynamics and a one-to-one correspondence between the *impact parameter*, b and θ_R given by

$$b = d\cos(\theta_R/2) \tag{53}$$

provided $b \leq d$. If $b > d$, then we have $\theta_R = 0$.

For hard-sphere scattering, do not confuse the *classical* DCS of eqn (52) with the *quantum diffraction* DCS of eqn (38), as used in the theory of coronae.

Assumption 2. The role of the transferred atom is to determine which impact parameters lead to reaction. If we denote the *reaction probability distribution function* by $P(b)$, then the DCS for the SOM is obtained by multiplying $\sigma_{hs}(\theta_R)$ by the reaction probability distribution function:

$$\sigma_{SOM}(\theta_R) = (d/2)^2 P(b(\theta_R)) \tag{54}$$

provided $b \leq d$. If $b > d$, then $\sigma_{SOM}(\theta_R) \equiv 0$. Note that eqn (54) uses the classical hard-sphere relation of eqn (53).

To obtain $P(b)$, we assume that $b \approx J/k$. For the four state-to-state reactions that we analyse in Section 13, we always have $j_i = 0$, thereby justifying this approximation, which neglects the difference between total and orbital angular momentum. We can now write, $P(b) \approx P_J \equiv P(J)$, so that

$$\sigma_{SOM}(\theta_R) = (d/2)^2 P(J(\theta_R)) \tag{55}$$

with

$$J(\theta_R) = kd\cos(\theta_R/2) \tag{56}$$

Here $J \leq kd$; otherwise, $\sigma_{SOM}(\theta_R) \equiv 0$.

The two assumptions of the SOM imply that, in practice, it should work best for rebound collisions. These result from a repulsive interaction between the reacting partners, which gives rise to predominantly backward scattering. Notice that d is the only adjustable parameter in the SOM model.

13. SOM results:DCSs at intermediate and backward angles

The DCSs calculated using the SOM are shown in Fig. 10 for the four transitions. The abscissae on the graphs go from $\theta_R = 50°$ to $\theta_R = 180°$, thereby providing overlap with Fig. 9. For each transition, two SOM DCS curves are shown.

For the first curve, d is chosen to fit approximately the first minimum in the slow frequency oscillations of the PWS DCS, as θ_R moves down from $\theta_R = 180°$. This first SOM DCS is drawn as a red *solid* curve. The fit used the Manipulate[•] command in *Mathematica 12.1.1*. For the second curve, the previous SOM DCS has been scaled to the value of the PWS DCS at $\theta_R = 180°$. We call this second fit, SOM(scaled), and the corresponding DCS is drawn as a red *dashed* curve in Fig. 10.

Next we compare the SOM DCSs with the PWS DCSs. We observe satisfactory agreement with the PWS DCSs for $\theta_R \gtrsim 50°$, which includes the flattish PWS DCS at intermediate scattering angles. These results are encouraging considering the simplicity of the SOM, with eqn (55) and (56) telling us that

13364 | *Phys. Chem. Chem. Phys.*, 2021, **23**, 13349–13369

This journal is © the Owner Societies 2021

Fig. 10 Plots of $\sigma(\theta_R)$ versus θ_R at $E_{trans} = 1.35$ eV for the angular range, $\theta_R = 50°$ to $\theta_R = 180°$. The DCSs plotted are: PWS (black solid curve), SOM (red solid curve), SOM/scaled at $\theta_R = 180°$ (red dashed curve). The transitions are: (a) 000 → 000 using $d = 1.71\ a_0$, (b) 000 → 010 using $d = 1.80\ a_0$, (c) 000 → 020 using $d = 1.90\ a_0$, (d) 000 → 030 using $d = 1.80\ a_0$.

the SOM and PWS DCSs are distorted mirror images of the corresponding P_J versus J plots.

In more detail, we see the SOM(scaled) DCS agrees closely with the backward peak in the PWS DCS for all four transitions, whilst the SOM shows reasonable agreement with the first minimum *and* the first maximum, as we move to smaller angles away from the backward direction. As expected, the SOM nor SOM(scaled) does not reproduce the oscillatory PWS DCSs for $\theta_R \lesssim 50°$ (not shown).

The values of d for the 000, 010, 020, 030 cases are similar, being $d/a_0 = 1.71, 1.80, 1.90, 1.80$, respectively. Note that the corresponding values of kd, which are used in eqn (56), are 20.0, 21.0, 22.2, 21.0. We can also compare the values of d with the saddle point properties of the BKMP2 potential energy surface. Now BKMP2 has a collinear symmetric saddle point with $r_{HH}^{\ddagger} = 1.757\ a_0$ and $r_{HD}^{\ddagger} = 1.757\ a_0$, so that $d^{\ddagger} = r_{HH}^{\ddagger} + r_{HD}^{\ddagger} = 3.514\ a_0$.[46] We observe that all four d values satisfy $d < d^{\ddagger}$. This result is consistent with the backward scattering arising from small impact parameters – or equivalently small values of J – rather than being determined by the saddle point geometry.

14. Conclusions

We have investigated quantitatively the angular scattering dynamics of the state-to-state reaction, H + HD($v_i = 0$, $j_i = 0$, $m_i = 0$) → H$_2$($v_f = 0$, $j_f = 0,1,2,3$, $m_f = 0$) + D for the whole range of angles from $\theta_R = 0°$ to $\theta_R = 180°$. The restriction to $m_f = 0$ arose because states with $m_f \neq 0$ have DCSs that are identically zero in the forward ($\theta_R = 0°$) and backward ($\theta_R = 180°$) directions. The input to our analyses consisted of accurate quantum scattering matrix elements computed by Yuan *et al.* for the BKMP2 potential energy surface at a translational energy of 1.35 eV. The theoretical techniques used were: full and N, F PWS and LAMs, including resummations of the full PWS, up to $r = 3$. We also used tPWS arising from window representations of the scattering matrix.

To investigate the asymptotic limits of the Legendre PWS, we employed six SC small-angle glory theories and four N rainbow theories. We introduced CoroGlo tests in order to distinguish between corona and glory scattering at small angles. Finally, we used the SOM theory of Herschbach to understand structure in the DCSs at intermediate and large angles.

We reached the following conclusions:

● The small-angle peaks in the DCSs come mainly from forward glory scattering. For the 020 case, there is also a contribution from a broad N rainbow.

● At larger angles, the fast oscillations in the DCSs arise from NF interference. The N scattering contains a broad, or hidden, rainbow for the 000, 020, 030 cases. For the 000 → 020 transition, the rainbow extends up to $\theta_R \approx 60°$; for the 000 and 030 cases, the angular ranges exhibiting a N rainbow are smaller.

● The periods of the fast NF oscillations can be used to estimate J_g.

● At intermediate and backward angles, the slowly varying DCSs, which merge into slow oscillations, are explained by the

This journal is © the Owner Societies 2021

Phys. Chem. Chem. Phys., 2021, **23**, 13349–13369 | **13365**

SOM. Physically it shows that structure in a DCS is a distorted mirror image of the corresponding P_J versus J plot.

Conflicts of interest

There are no conflicts to declare.

Appendix

In this appendix, we discuss how a resummation affects the N and F scattering subamplitudes for a window representation of the S matrix, which in turn gives rise to a truncated PWS. To make this Appendix self-contained, we first recall the following results for the resummation of the full scattering amplitude, where we write $r = 0$ for the un-resummed amplitude. We have

$$f_{r=0}(\theta_R) = \frac{1}{2ik} \sum_{J=0}^{\infty} a_J^{(r=0)} P_J(\cos \theta_R) \tag{A1}$$

with

$$a_J^{(r=0)} = (2J + 1)\tilde{S}_J \quad J = 0,1,2,\ldots \tag{A2}$$

In practice, the infinite upper limit in eqn (A1) is usually replaced by a finite cut-off value, J_{max}, on the assumption that all partial waves with $J > J_{max}$ are negligible.

It is known that a single resummation, $r = 1$, applied to eqn (A1) and (A2) gives[13–19]

$$f_{r=1}(\theta_R) = \frac{1}{2ik} \frac{1}{(1 + \beta_1 \cos \theta_R)} \sum_{K=0}^{\infty} a_K^{(r=1)}(\beta_1) P_K(\cos \theta_R) \tag{A3}$$

provided $1 + \beta_1 \cos \theta_R \neq 0$, where $\beta_1 \equiv \beta_1^{(r=1)}$ is the real-, or complex-, valued resummation parameter, and

$$a_K^{(r=1)}(\beta_1) = \beta_1 \frac{K}{2K - 1} a_{K-1}^{(r=0)} + a_K^{(r=0)} + \beta_1 \frac{K + 1}{2K + 3} a_{K+1}^{(r=0)} \quad K = 0, 1, 2, \ldots \tag{A4}$$

with $a_{K=-1}^{(r=0)} = 0$. Notice in eqn (A3) and (A4), we have used K, rather than J, for the summation index, as a reminder that K should not be interpreted as the total angular momentum quantum number, because the factor $(1 + \beta_1 \cos \theta_R)^{-1}$ has been removed from the PWS.[13]

The N, F $r = 1$ resummed subamplitudes are given by (with $\theta_R \neq 0, \pi$ for the Fuller decomposition):[13–19]

$$f_{r=1}^{(N,F)}(\beta_1; \theta_R) = \frac{1}{2ik} \frac{1}{(1 + \beta_1 \cos \theta_R)} \sum_{K=0}^{\infty} a_K^{(r=1)}(\beta_1) Q_K^{(N,F)}(\cos \theta_R) \tag{A5}$$

where

$$Q_K^{(N,F)}(\cos \theta_R) = \frac{1}{2} \left[P_K(\cos \theta_R) \pm \frac{2i}{\pi} Q_K(\cos \theta_R) \right] \quad K = 0, 1, 2, \ldots$$

An alternative form of eqn (A5) is the identity[13,19]

$$f_{r=1}^{(N,F)}(\beta_1; \theta_R) = f_{r=0}^{(N,F)}(\theta_R) \mp \frac{1}{2\pi k} \frac{\beta_1 a_{J=0}^{(r=0)}}{(1 + \beta_1 \cos \theta_R)} \tag{A6}$$

In applications of eqn (A3)–(A6), it is necessary to choose a value for β_1. We usually adopt the suggestion of Anni et al.[13] and solve the equation $a_{K=0}^{(r=1)}(\beta_1) = 0$ to determine β_1. This gives

$$\beta_1 = -3 \frac{a_{J=0}^{(r=0)}}{a_{J=1}^{(r=0)}} = -\frac{\tilde{S}_{J=0}}{\tilde{S}_{J=1}} \tag{A7}$$

Definition. A window representation of the S matrix employs a finite proper subset of non-zero elements taken from the set $\{\tilde{S}_J | J = 0,1,2,\ldots,J = J_{max}\}$. In our applications, we use as a window the subset $\{\tilde{S}_J | J = 0 \leq J_i < J_f \leq J = J_{max}\}$, and exclude the case where both $J_i = 0$ and $J_f = J_{max}$. Typically, the values of J from $J = J_i$ to $J = J_f$ are chosen so that the corresponding $\{\tilde{S}_J\}$ reproduce some important aspect(s) of the angular scattering.

Remark. When we have a full PWS with $J_i = 0$ and $J_f = J_{max}$, the term "window representation" is also used in the literature in a different, although related, context.[19,88,89] It is used when an exact rearrangement of the full PWS results in the main numerical contribution coming from a subset of S matrix elements – also called the window region.[19,88,89]

Using the definition above, we can now write the window scattering amplitude for $r = 0$ as

$$f_{r=0}^{wind}(\theta_R) = \frac{1}{2ik} \sum_{J=J_i}^{J=J_f} a_J^{(r=0)} P_J(\cos \theta_R) \tag{A8}$$

We want to use eqn (A6) relating the N, F scattering subamplitudes for $r = 1$ to those for $r = 0$, but the summation limits in eqn (A8) are not the same as those in eqn (A1). To overcome this difficulty, we define new coefficients which are zero for $J < J_i$ and $J > J_f$

$$\begin{cases} c_0^{(r=0)} = c_1^{(r=0)} = \cdots = c_{J_i-1}^{(r=0)} \equiv 0 \\ c_{J_i}^{(r=0)} = a_{J_i}^{(r=0)}, c_{J_i+1}^{(r=0)} = a_{J_i+1}^{(r=0)}, \cdots, c_{J_f}^{(r=0)} = a_{J_f}^{(r=0)} \\ c_{J_f+1}^{(r=0)} = c_{J_f+2}^{(r=0)} = \cdots \equiv 0 \end{cases} \tag{A9}$$

In eqn (A9), we have assumed that $J_i \geq 1$. Then it is clear we can write eqn (A8) as

$$f_{r=0}^{wind}(\theta_R) = \frac{1}{2ik} \sum_{J=0}^{\infty} c_J^{(r=0)} P_J(\cos \theta_R) \tag{A10}$$

since the coefficients equal to zero do not contribute. We can now apply eqn (A3) and (A4) to eqn (A10) obtaining

$$f_{r=1}^{wind}(\theta_R) = \frac{1}{2ik} \frac{1}{(1 + \beta_1 \cos \theta_R)} \sum_{K=0}^{\infty} c_K^{(r=1)}(\beta_1) P_K(\cos \theta_R) \tag{A11}$$

where

$$c_K^{(r=1)}(\beta_1) = \beta_1 \frac{K}{2K - 1} c_{K-1}^{(r=0)} + c_K^{(r=0)} + \beta_1 \frac{K + 1}{2K + 3} c_{K+1}^{(r=0)} \quad K = 0, 1, 2, \ldots \tag{A12}$$

with $c_{K=-1}^{(r=0)} = 0$. Next we ask the question: which $c_K^{(r=1)}(\beta_1)$ are non-zero in eqn (A12)? Inspection of eqn (A9) and (A12) shows

13366 | Phys. Chem. Chem. Phys., 2021, **23**, 13349–13369

This journal is © the Owner Societies 2021

that the summation in eqn (A11) can be restricted to $J_i - 1$ up to $J_f + 1$, since the other coefficients are null. We can now write

$$f_{r=1}^{\text{wind}}(\theta_R) = \frac{1}{2ik} \frac{1}{(1 + \beta_1 \cos \theta_R)} \sum_{K=J_i-1}^{K=J_f+1} c_K^{(r=1)}(\beta_1) P_K(\cos \theta_R)$$

We next apply the identity (A6) to eqn (A11), which gives for the N, F $r = 1$ subamplitudes

$$f_{r=1}^{(\text{N,F})}(\beta_1; \theta_R) = f_{r=0}^{(\text{N,F})}(\theta_R) \mp \frac{1}{2\pi k} \frac{\beta_1 c_{J=0}^{(r=0)}}{(1 + \beta_1 \cos \theta_R)}$$

Now from eqn (A9) with $J_i \geq 1$, we see that $c_{J=0}^{(r=0)} = 0$. So the above equation simplifies to

$$f_{r=1}^{\text{wind,(N,F)}}(\beta_1; \theta_R) = f_{r=0}^{\text{wind,(N,F)}}(\theta_R) \qquad \text{(A13)}$$

Eqn (A13) tells us that a $r = 1$ resummation for the window case with $J_i \geq 1$ does not change the values of the N, F subamplitudes compared to the $r = 0$ un-resummed window case. This useful property allows us to check computer codes and numerical procedures.

When performing computations, we need a value for β_1. By analogy with the Anni *et al.* prescription,[13] we determine β_1 when $J_i \geq 1$ by solving $c_{K=J_i}^{(r=1)}(\beta_1) = 0$, which leads to

$$\beta_1 = -\frac{(2J_i + 3)}{J_i + 1} \frac{c_{J=J_i}^{(r=0)}}{c_{J=J_i+1}^{(r=0)}} = -\frac{(2J_i + 1)}{J_i + 1} \frac{\tilde{S}_{J=J_i}}{\tilde{S}_{J=J_i+1}} \qquad \text{(A14)}$$

Notice that the numerical value for β_1 from eqn (A14) where $J_i \geq 1$ is different from eqn (A7) where $J_i = 0$.

Finally we note that the results presented above can be generalized to resummation orders, $r = 2, 3, 4, \ldots$ with resummation parameters $\{\beta_1^{(r=2)}, \beta_2^{(r=2)}\}$, $\{\beta_1^{(r=3)}, \beta_2^{(r=3)}, \beta_3^{(r=3)}\}$, $\{\beta_1^{(r=4)}, \beta_2^{(r=4)}, \beta_3^{(r=4)}, \beta_4^{(r=4)}\}\ldots$, provided that $J_i \geq 2$, $J_i \geq 3$, $J_i \geq 4, \ldots$ respectively.

Acknowledgements

References

1 W. Hu and G. C. Schatz, *J. Chem. Phys.*, 2006, **125**, 132301.

2 A. Laganà and G. A. Parker, *Chemical Reactions: Basic Theory and Computing*, Springer International Publishing, Cham, Switzerland, 2018.

3 N. E. Henriksen and F. Y. Hansen, *The Microscopic Foundation of Chemical Kinetics*, Oxford University Press, Oxford, UK, 2nd edn, 2019.

4 M. S. Child, *Semiclassical Mechanics with Molecular Applications*, Oxford University Press, Oxford, UK, 2nd edn, 2014.

5 D. Yuan, S. Yu, W. Chen, J. Sang, C. Luo, T. Wang, X. Xu, P. Casavecchia, X. Wang, Z. Sun, D. H. Zhang and X. Yang, *Nat. Chem.*, 2018, **10**, 653.

6 J. Sang, D. Yuan, W. Chen, S. Yu, C. Luo, S. Wang, T. Wang, X. Yang and X. Wang, *Chin. J. Chem. Phys.*, 2019, **32**, 123.

7 D. Yuan, Y. Guan, W. Chen, H. Zhao, S. Yu, C. Luo, Y. Tan, T. Xie, X. Wang, Z. Sun, D. H. Zhang and X. Yang, *Science*, 2018, **362**, 1289.

8 Y. Xie, H. Zhao, Y. Wang, Y. Huang, T. Wang, X. Xu, C. Xiao, Z. Sun, D. H. Zhang and X. Yang, *Science*, 2020, **368**, 767.

9 D. Yuan, Y. Huang, W. Chen, H. Zhao, S. Yu, C. Luo, Y. Tan, S. Wang, X. Wang, Z. Sun and X. Yang, *Nat. Commun.*, 2020, **11**, 3640.

10 J. N. L. Connor, P. McCabe, D. Sokolovski and G. C. Schatz, *Chem. Phys. Lett.*, 1993, **206**, 119.

11 P. McCabe and J. N. L. Connor, *J. Chem. Phys.*, 1996, **104**, 2297.

12 A. J. Dobbyn, P. McCabe, J. N. L. Connor and J. F. Castillo, *Phys. Chem. Chem. Phys.*, 1999, **1**, 1115. On p. 1118, in eqn (18), for "θ)", read "θ". On p. 1119, one line below eqn (31), for "$I_{v_f j_f m_{f-} v_i j_i m_i}(\theta_R)$" read "$I_{v_f j_f m_{f-} v_i j_i m_i}^{\text{opt}}(\theta_R)$". On p. 1123, for "H + D$_2$ + HD + D", read "H + D$_2$ → HD + D".

13 R. Anni, J. N. L. Connor and C. Noli, *Phys. Rev. C: Nucl. Phys.*, 2002, **66**, 044610.

14 C. Noli and J. N. L. Connor, *Russ. J. Phys. Chem.*, 2002, **76**(Supplement 1), S77. Also available at: https://arXiv.org/abs/physics/0301054.

15 R. Anni, J. N. L. Connor and C. Noli, *Khim. Fiz.*, 2004, **23**(2), 6. Also available at: https://arXiv.org/abs/physics/0410266.

16 J. N. L. Connor and R. Anni, *Phys. Chem. Chem. Phys.*, 2004, **6**, 3364.

17 J. J. Hollifield and J. N. L. Connor, *Phys. Rev. A: At., Mol., Opt. Phys.*, 1999, **59**, 1694.

18 J. J. Hollifield and J. N. L. Connor, *Mol. Phys.*, 1999, **97**, 293.

19 A. J. Totenhofer, C. Noli and J. N. L. Connor, *Phys. Chem. Chem. Phys.*, 2010, **12**, 8772.

20 X. Shan and J. N. L. Connor, *Phys. Chem. Chem. Phys.*, 2011, **13**, 8392.

21 X. Shan and J. N. L. Connor, *J. Phys. Chem. A*, 2012, **116**, 11414.

22 X. Shan and J. N. L. Connor, *J. Phys. Chem. A*, 2014, **118**, 6560.

23 D. Sokolovski, *Chem. Phys. Lett.*, 2003, **370**, 805.

24 J. N. L. Connor, *Phys. Chem. Chem. Phys.*, 2004, **6**, 377.

25 J. N. L. Connor, *Mol. Phys.*, 2005, **103**, 1715.

26 C. Xiahou and J. N. L. Connor, *Mol. Phys.*, 2006, **104**, 159.

27 C. Xiahou, J. N. L. Connor and D. H. Zhang, *Phys. Chem. Chem. Phys.*, 2011, **13**, 12981.

28 C. Xiahou and J. N. L. Connor, *Phys. Chem. Chem. Phys.*, 2014, **16**, 10095.

29 (*a*) R. Greenler, *Rainbows, Halos and Glories*, SPIE, Bellingham, Washington, USA, 2020, ch. 6; (*b*) See also: R. Greenler, *Chasing the Rainbow. Recurrences in the Life of a Scientist*, Elton-Wolf Publishing: Milwaukee, Wisconsin, USA, 2000.

This journal is © the Owner Societies 2021

Phys. Chem. Chem. Phys., 2021, **23**, 13349–13369 | **13367**

30 G. P. Können, *Bull. Am. Meteorol. Soc.*, 2017, **98**, 485.

31 J. A. Shaw, *Optics in the Air: Observing Optical Phenomena through Airplane Windows*, SPIE: Bellingham, Washington, USA, 2017, Chap. 3.

32 P. Laven, in *The Mie Theory: Basics and Applications*, eds. W. Hergert and T. Wriedt, *Springer Series in Optical Sciences*, 2012, **169**, 193.

33 L. Cowley, P. Laven and M. Vollmer, *Phys. Educ.*, 2005, **40**, 51.

34 (*a*) J. N. L. Connor and R. A. Marcus, *J. Chem. Phys.*, 1971, **55**, 5636; (*b*) For a commentary, see: J. N. L. Connor, *Curr. Contents, Phys. Chem. Earth Sci.*, 1991, **31**(50), 10; (*c*) J. N. L. Connor, *Curr. Contents, Eng. Technol. Appl. Sci.*, 1991, **22**(50), 10. Also available at http://garfield.library.upenn.edu/classics1991/A1991GR14400001.pdf.

35 D. R. Herschbach, *Appl. Opt.*, 1965, **4**(S1), 128.

36 D. R. Herschbach, *Adv. Chem. Phys.*, 1966, **10**, 319.

37 H. Zhao, X. Hu, D. Xie and Z. Sun, *J. Chem. Phys.*, 2018, **149**, 174103.

38 Z. Sun, H. Guo and D. H. Zhang, *J. Chem. Phys.*, 2010, **132**, 084112.

39 H. Zhao, U. Umer, X. Hu, D. Xie and Z. Sun, *J. Chem. Phys.*, 2019, **150**, 134105.

40 S. D. Chao, S. A. Harich, D. X. Dai, C. C. Wang, X. Yang and R. T. Skodje, *J. Chem. Phys.*, 2002, **117**, 8341.

41 S. A. Harich, D. Dai, C. C. Wang, X. Yang, S. D. Chao and R. T. Skodje, *Nature*, 2002, **419**, 281.

42 S. A. Harich, D. Dai, X. Yang, S. D. Chao and R. T. Skodje, *J. Chem. Phys.*, 2002, **116**, 4769.

43 R. C. Fuller, *Phys. Rev. C: Nucl. Phys.*, 1975, **12**, 1561.

44 P. J. Hatchell, *Phys. Rev. C: Nucl. Phys.*, 1989, **40**, 27.

45 K.-E. Thylwe and P. McCabe, *J. Math. Chem.*, 2017, **55**, 1638.

46 A. I. Boothroyd, W. J. Keogh, P. G. Martin and M. R. Peterson, *J. Chem. Phys.*, 1996, **104**, 7139.

47 D. Sokolovski, J. N. L. Connor and G. C. Schatz, *J. Chem. Phys.*, 1995, **103**, 5979.

48 H. M. Nussenzveig, *Sci. Am.*, 2012, **306**, 68.

49 J. A. Adam, *Phys. Rep.*, 2002, **356**, 229.

50 D. Sokolovski, D. De Fazio, S. Cavalli and V. Aquilanti, *Phys. Chem. Chem. Phys.*, 2007, **9**, 5664.

51 X. Shan and J. N. L. Connor, *J. Chem. Phys.*, 2012, **136**, 044315.

52 J. N. L. Connor, *Mol. Phys.*, 1976, **31**, 33.

53 L. F. Canto and M. S. Hussein, *Scattering Theory of Molecules, Atoms and Nuclei*, World Scientific, Singapore (2013). In eqn (5.396) and neighbouring equations, the factor "$\sin\theta/\theta$" should be "$\theta/\sin\theta$".

54 M. Flannery, in *Springer Handbook of Atomic, Molecular and Optical Physics*, ed. G. W. F. Drake, Springer-Verlag: New York, USA, 2006, Part D, Chap. 45, eqn (45.145).

55 P. Laven, *Appl. Opt.*, 2015, **54**, B46.

56 J. A. Adam, *Rays, Waves and Scattering: Topics in Classical Mathematical Physics*, Princeton University Press: Princeton, New Jersey, USA, 2017, p. 411.

57 D. M. Brink, *Semi-Classical Methods for Nucleus-Nucleus Scattering*, Cambridge University Press: Cambridge, UK, 1985.

58 W. T. Grandy, Jr., *Scattering of Waves from Large Spheres*, Cambridge University Press: Cambridge, UK, 2000. In Fig. 2.4, the factor "4" in the label on the ordinate should read "2".

59 H. M. Nussenzveig, *Diffraction Effects in Semiclassical Scattering*, Cambridge University Press: Cambridge, UK, 1992.

60 F. Bowman, *Introduction to Bessel Functions*, Dover Publications, New York, NY, USA (1958), p. 127. This Dover edition is an unabridged and unaltered republication of the first edition originally published in 1938 by Longmans & Co, London, UK.

61 W. W. Bell, *Special Functions for Scientists and Engineers*, Dover Publications, Mineola, New York, USA (2004), p. 127, Theorem 4.21. This Dover edition is an unabridged republication of the work originally published in 1968 by D. Van Nostrand Company, Ltd., London, England.

62 J. N. L. Connor and D. C. Mackay, *Mol. Phys.*, 1979, **37**, 1703.

63 J. N. L. Connor, in *Semiclassical Methods in Molecular Scattering and Spectroscopy*, Proceedings of the NATO Advanced Study Institute held in Cambridge, England in September 1979, ed. M. S. Child, Reidel, Dordrecht, Netherlands, 1980, pp. 45–107.

64 X. Shan, C. Xiahou and J. N. L. Connor, *Phys. Chem. Chem. Phys.*, 2018, **20**, 819.

65 C. Xiahou, X. Shan and J. N. L. Connor, *Phys. Scr.*, 2019, **94**, 065401.

66 C. Xiahou and J. N. L. Connor, *J. Phys. Chem. A*, 2009, **113**, 15298.

67 D. M. Neumark, A. M. Wodtke, G. N. Robinson, C. C. Hayden and Y. T. Lee, *J. Chem. Phys.*, 1985, **82**, 3045.

68 X. Wang, W. Dong, M. Qiu, Z. Ren, L. Che, D. Dai, X. Wang, X. Yang, Z. Sun, B. Fu, S.-Y. Lee, X. Xu and D. H. Zhang, *Proc. Natl. Acad. Sci. U. S. A.*, 2008, **105**, 6227.

69 J. N. L. Connor and D. Farrelly, *J. Chem. Phys.*, 1981, **75**, 2831.

70 N. Nešković, ed., *Rainbows and Catastrophes*, Proceedings of the Workshop on Rainbow Scattering, Cavtat, Yugoslavia, Boris Kidrić Institute of Nuclear Science, Belgrade, Yugoslavia, 1990.

71 D. Sokolovski and A. Z. Meszane, *Phys. Rev. A: At., Mol., Opt. Phys.*, 2004, **70**, 032710.

72 H. Pan and K. Liu, *J. Phys. Chem. A*, 2016, **120**, 6712.

73 N. Nešković, S. Petrović and M. Ćosić, eds., *Rainbows in Channeling of Charged Particles in Crystals and Nanotubes, Lecture Notes in Nanoscale Science and Technology*, 2017, **25**.

74 S. Mondal, S. Bhattacharyya and K. Liu, *Mol. Phys.*, 2020, **119**, DOI: 10.1080/00268976.2020.1766706.

75 H. Pan, S. Liu, D. H. Zhang and K. Liu, *J. Phys. Chem. Lett.*, 2020, **11**, 9446.

76 J. L. Kinsey, G. H. Kwei and D. R. Herschbach, *J. Chem. Phys.*, 1976, **64**, 1914.

77 G. H. Kwei and D. R. Herschbach, *J. Phys. Chem.*, 1979, **83**, 1550.

78 M. L. Vestal, A. L. Wahrhaftig and J. H. Futrell, *J. Phys. Chem.*, 1976, **80**, 2892.

79 M. A. Collins and R. G. Gilbert, *Chem. Phys. Lett.*, 1976, **41**, 108.

80 S. M. McPhail and R. G. Gilbert, *Chem. Phys.*, 1978, **34**, 319.

81 N. Agmon, *Chem. Phys.*, 1981, **61**, 189.

13368 | *Phys. Chem. Chem. Phys.*, 2021, **23**, 13349-13369

This journal is © the Owner Societies 2021

82 N. Agmon, *Int. J. Chem. Kinet.*, 1986, **18**, 1047.

83 R. E. Wyatt, J. F. McNutt and M. J. Redmon, *Ber. Bunsenges. Phys. Chem.*, 1982, **86**, 437.

84 G. C. Schatz, B. Amaee and J. N. L. Connor, *Comput. Phys. Commun.*, 1987, **47**, 45.

85 G. C. Schatz, B. Amaee and J. N. L. Connor, *J. Phys. Chem.*, 1988, **92**, 3190.

86 G. C. Schatz, B. Amaee and J. N. L. Connor, *J. Chem. Phys.*, 1990, **93**, 5544.

87 G. C. Schatz, D. Sokolovski and J. N. L. Connor, *Faraday Discuss. Chem. Soc.*, 1991, **91**, 17.

88 N. Rowley, *J. Phys. G: Nucl. Phys.*, 1980, **6**, 697.

89 J. N. L. Connor and K.-E. Thylwe, *J. Chem. Phys.*, 1987, **86**, 188.

This journal is © the Owner Societies 2021

Phys. Chem. Chem. Phys., 2021, **23**, 13349–13369 | **13369**